JOURNAL OF GUIDANCE, CONTROL, AND DYNAMICS
Vol. 34, No. 2, March–April 2011

Hypersonic State Estimation Using the Frobenius–Perron Operator

Parikshit Dutta* and Raktim Bhattacharya†
Texas A&M University, College Station, Texas 77843-3141

DOI: 10.2514/1.52184

This paper presents a nonlinear state-estimation algorithm that combines the Frobenius–Perron operator theory with the Bayesian estimation theory. The Frobenius–Perron operator is used to predict evolution of uncertainty in the nonlinear system and obtain the prior probability density function in the estimation process. The Bayesian update rule is used to determine the posterior density function from the available measurements. The framework for this filter is similar to particle filters where the density function is sampled using a cloud of points and the system dynamics are integrated with these points as the initial condition. The key issue in particle filters is that the weight for the sample points are typically determined using histograms to obtain the prior density function, and thus requires many samples for acceptable accuracy. Moreover, the weights of the majority of the particles converge to zero after a few iterations, rendering them useless for state-estimation purposes. This issue can be resolved with the application of the Frobenius–Perron operator, which determines the time evolution of the weights along sample paths. This greatly simplifies the determination of the prior density function and can be achieved with fewer sample points. Consequently, the associated computational time is also greatly reduced. The presented algorithm is demonstrated on a hypersonic reentry problem with uncertain initial states, with given initial probability density functions. The performance is compared with particle filters, and it is observed that the proposed algorithm is computationally superior as expected.

I. Introduction

ENTRY, descent, and landing of a hypersonic vehicle on the surface of Mars is a topic of research receiving much attention in recent years. The expected mass of the next Mars Science Laboratory Mission is approximately 2800 kg at entry, which is required to land within a few kilometers of robotic test sites. The requirement of high accuracy when landing in proximity of the target region is a key challenge of high mass entry. It is therefore necessary to estimate states and parameters of the reentry vehicle when uncertainties are present in initial conditions. High nonlinearity of reentry dynamics, coupled with a lack of frequent sensor updates, makes the estimation problem difficult to solve. Sequential estimation algorithms based on Monte Carlo (MC) simulations are most commonly used in such cases. However, for systems having three or more dimensions, MC-based techniques may be computationally expensive, as the ensemble size required to guarantee convergence increases exponentially with the number of states. The objective of this paper is to demonstrate the application of a new nonlinear estimation algorithm to hypersonic flight problems and highlight its superiority, in terms of error convergence and computational efficiency, over the popular particle-filtering-based methods.

Estimation of states and parameters for dynamical systems, in general, is generally performed in the Bayesian framework, where uncertainty is represented as probability density functions (PDFs). For linear Gaussian systems, it is possible to get exact analytical expressions for the evolving sequence of moments, which characterizes the PDF completely. This method is widely known as the Kalman filter [1]. For nonlinear systems exhibiting Gaussian behavior, the system is linearized locally, about the current mean, and the covariance is propagated using the approximated linear dynamics. This method is used in extended Kalman filters (EKFs) [2]. It is well known that this approach performs poorly when the nonlinearities are high, resulting in an unstable estimator [3–6]. However, the error in mean and covariance can be reduced if the uncertainty is propagated, using nonlinear dynamics, for a minimal set of sample points called sigma points. The PDF of the states, characterized by sigma points, captures the posterior mean and covariance accurately to the third order (Taylor-series expansion) for any nonlinearity with Gaussian behavior. This technique has resulted in the unscented Kalman filter (UKF) [7]. The aforementioned filters are based on the premise of Gaussian PDF evolution. If the sensor updates are frequent, then the EKF and UKF may yield satisfactory results. However, for nonlinear systems, if the sensor updates are slow, these filters result in inaccurate estimates [8].

Recently, simulation-based sequential filtering methods, using MC simulations, have been developed to tackle nonlinear systems with non-Gaussian uncertainty [9,10]. MC methods involve representing the PDF of the states using a finite number of samples. The filtering task is obtained by recursively generating properly weighted samples of the state variable using importance sampling [11]. These filters, based on sequential MC methods, are known as MC filters [12]. Among them, the most widely used is the particle filter [13–16]. Here, ensemble members or particles are propagated using nonlinear system dynamics. These particles with proper weights, determined from the measurements, are used to obtain the state estimate. However, it has been observed that the weights of most of the particles converge to zero after a few iterations. This, in effect, leads to extra computational effort spent on particles that do not contribute toward getting the state estimate. This phenomenon is called particle degeneracy [9]; hence, particle filters require a large number of ensembles for convergence, leading to higher computational costs [17]. This problem is tackled through resampling [8,13,18]. Particle filters with the resampling technique are commonly known as bootstrap filters [8]. It has been observed that bootstrap filters introduce other problems like loss of diversity among particles [15] if the resampling is not performed correctly. Recently developed techniques have combined importance sampling and Markov-chain–MC (MCMC) methods to generate samples to get better estimates of states and parameters [19]. Several other methods, like regularized particle filters [20] and filters involving the MCMC move step [21], have been developed to improve sample diversity. At the same time, even with resampling, due to the simulation-based nature of these filters, the ensemble size scales

Received 26 August 2010; revision received 23 November 2010; accepted for publication 27 November 2010.

*Graduate Student, Aerospace Engineering Department; p0d5585@aero.tamu.edu.

†Assistant Professor, Aerospace Engineering Department; raktim@aero.tamu.edu.

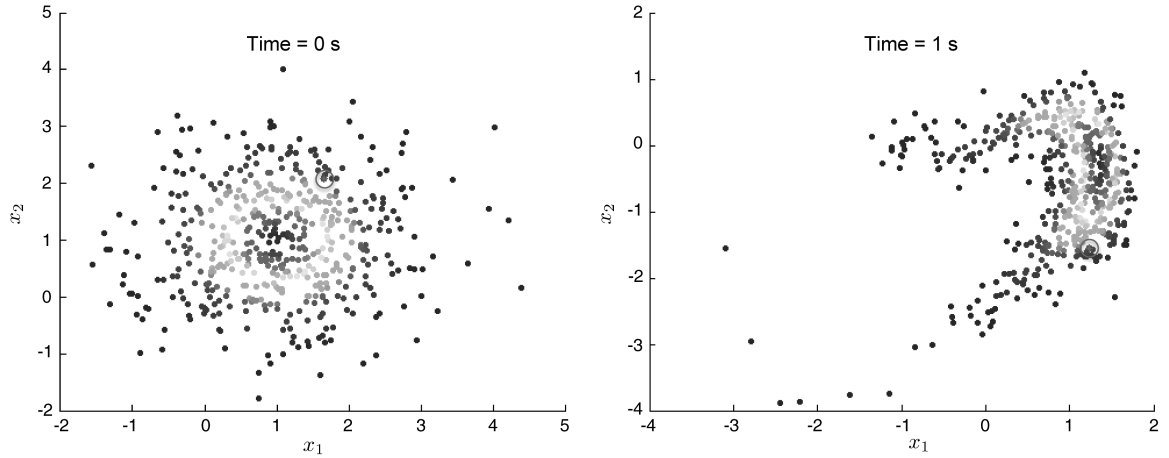

Fig. 1 Method of characteristics. Number of samples = 500. System shown is the Duffing oscillator. The circled area shows the location of sample points at two different time instances.

exponentially with the state dimension for large problems [22]. To circumvent this problem, particle filters based on Rao–Blackwellization have been developed to partially solve the estimation problem analytically [23]. However, its application is limited to systems where the required partition of the state space is possible. If the reader is interested, an excellent comparison of the various nonlinear filtering algorithms is available in [24].

As described previously, the main problem with particle filters is the determination of the weights for each sample. This greatly affects the accuracy. At the same time, for large-scale problems, the exponential growth in the number of samples makes this method computationally prohibitive. The problem of determining weights can be resolved by using the Frobenius–Perron (FP) operator. The FP operator has been used in the physics community to study the evolution of uncertainty in dynamical systems [25]. In continuous time, the FP operator is defined by the Liouville equation [26], which is the Fokker–Planck equation [27] without the diffusion term. It has been shown that the FP operator, or the Liouville equation, predicts evolution of uncertainty in a more computationally efficient manner than MC [28,29]. Based on this fact, we can expect a nonlinear

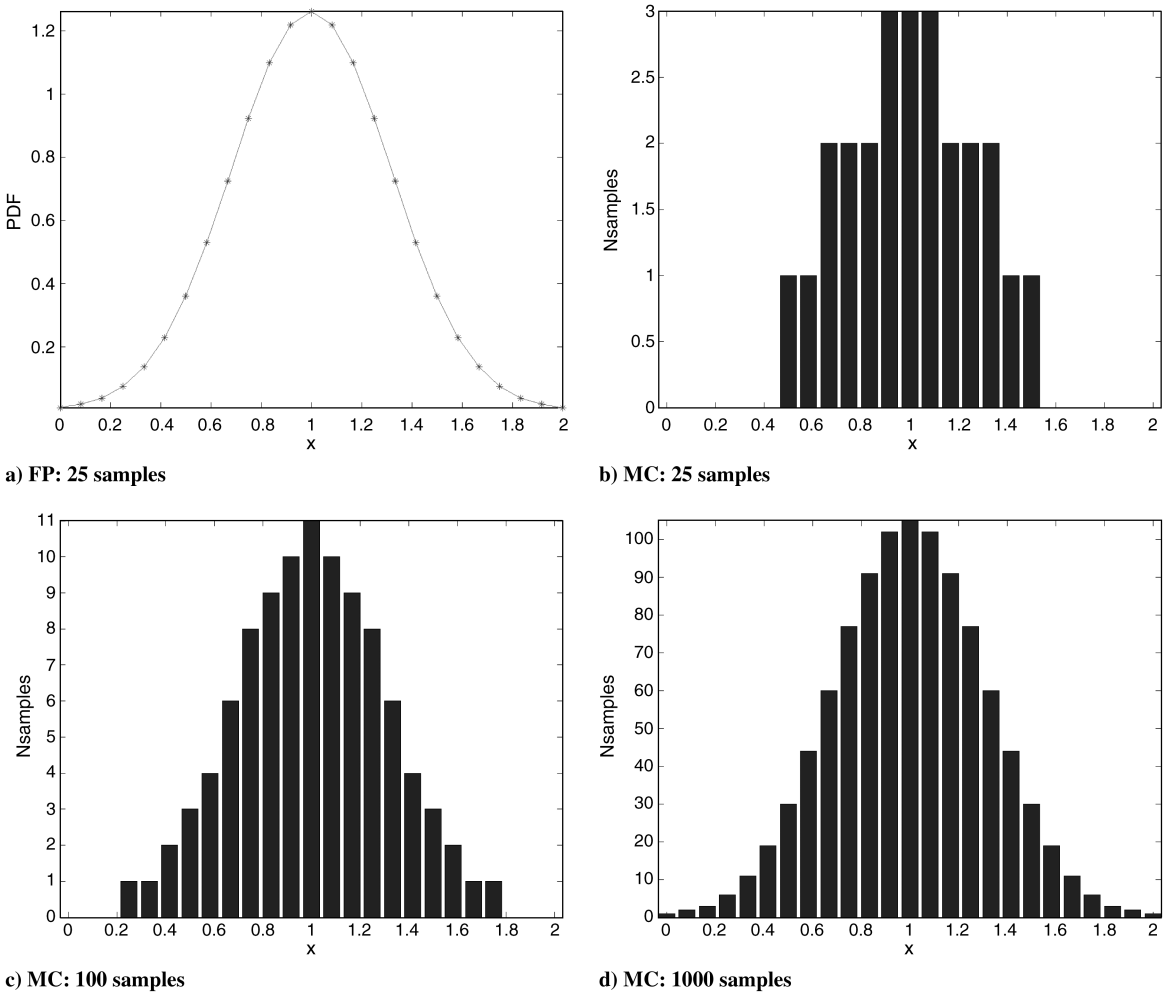

a) FP: 25 samples

b) MC: 25 samples

c) MC: 100 samples

d) MC: 1000 samples

Fig. 2 Comparison of FP- and MC-based approximations of density functions.

Table 1 Explanation and values of the constants for Martian atmosphere [46]

Description of constants	Value
Radius of Mars	$R_m = 3397 \times 10^3$ m
Acceleration due to gravity of Mars	$g = 3.71$ m/s^2
Ballistic coefficient of vehicle	$B_c = 72.8$ kg^2/m^2
Lift-to-drag ratio of vehicle	$\frac{L}{D} = 0.3$
Density at the surface of Mars	$\rho_0 = 0.0019$ kg/m^3
Scale height for density computation	$h_1 = 9.8$ km $h_2 = 20$ km
Escape velocity of Mars	$v_c = 5.027$ km/s

Table 2 Scaling constants for base units

Units	Scaling constants
Mass	Mass of vehicle = 2800 kg
Length	Radius of Mars R_m
Time	Radius of Mars/escape velocity of Mars = 675.7 s

Table 3 Normalization factors for measurements

Measurement	Normalization factors
Dynamic pressure	1.97×10^3 $\frac{\text{N}}{\text{m}}$
Heating rate	0.0231 $\frac{\text{J}}{\text{m-s}}$
Flight-path angle	19.13°

filtering algorithm in this framework to be computationally more efficient than particle filters. However, it is important to note that the FP operator only addresses parametric uncertainty. Use of the Liouville equation to develop a nonlinear filtering algorithm was first presented by Daum and Krichman [30], where the outline of the filtering algorithm has been presented. Subsequently, it has been shown that the FP operator-based filter can avoid particle degeneracy [24,31–33]. In this paper, this algorithm is applied to a state-estimation problem arising in hypersonic flights and performs a direct comparison with particle filters.

The paper is organized as follows. The particle-filtering algorithm is described first, followed by necessary background on the FP operator. Next, it is shown how this operator can be used to propagate parametric uncertainty. This is followed by the details of a nonlinear filtering algorithm using the FP operator and Bayesian theory. The filter is then applied to a hypersonic reentry flight dynamics problem, and its performance is compared with particle filters. Because of the similarity of the applied filter to particle filters, only the results between these two techniques are compared.

II. Particle Filter

Let us consider a nonlinear dynamical system with states $x \in \mathbb{R}^n$ and outputs $\tilde{y} \in \mathbb{R}^m$, for which the dynamics are given by

$$\dot{x} = g(x, \Delta) \tag{1a}$$

$$\tilde{y} = h(x) + \nu \tag{1b}$$

where ν is the measurement noise defined by $\nu \sim \mathcal{N}(0, R)$. Let Δ be a vector of random parameters. Let $p(\Delta)$ be the PDF of Δ and $\mathcal{D}_\Delta$ be the domain of Δ. Let us assume discrete measurement updates available at times $t_0, t_1, \cdots, t_k, \cdots$. Without loss of generality, it is assumed that the system has only initial condition uncertainty. Therefore, $\Delta := x$. Parameter estimation can be included in this framework by suitably augmenting the system. Note that process noise cannot be addressed in this framework. This is a limitation of the FP operator, or the Liouville equation. To include process noise, one has to solve the Fokker–Planck–Kolmogorov equation [27]. Our future work will address the solution of this equation for estimation purposes.

In brief, particle filters are based on the importance sampling theorem [11], where random samples are drawn from a given distribution at time t_{k-1}. Each sample point is assigned a weight that is determined from the distribution function. These sample points are taken as initial conditions for the dynamical system and evolved using Eq. (1a) to time t_k. Depending on their locations, the prior density function is approximated using histograms. The posterior density function is obtained using the corresponding likelihood function in a Bayesian setting. Based on the new density function, a new set of sample points are generated, and the process repeats.

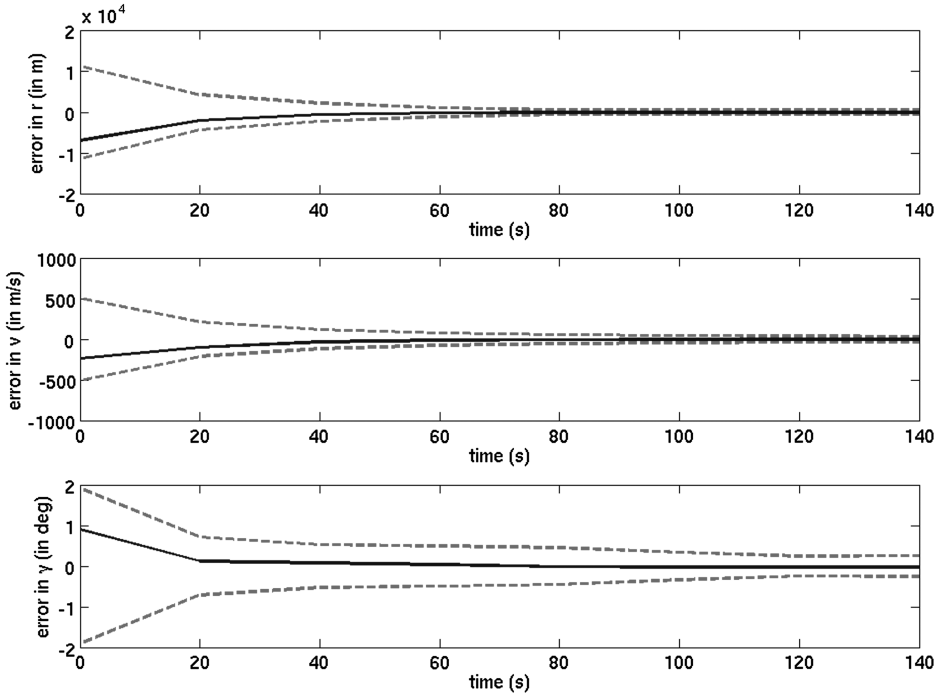

Fig. 3 Generic particle filter. True initial states are $[R_m + 61 \text{ km},\ 2.64 \text{ km/s} - 8.1°]^T$, and update interval is 20 s. The dashed lines represent $\pm 3\sigma$ limits, and the solid lines represent the error in estimation.

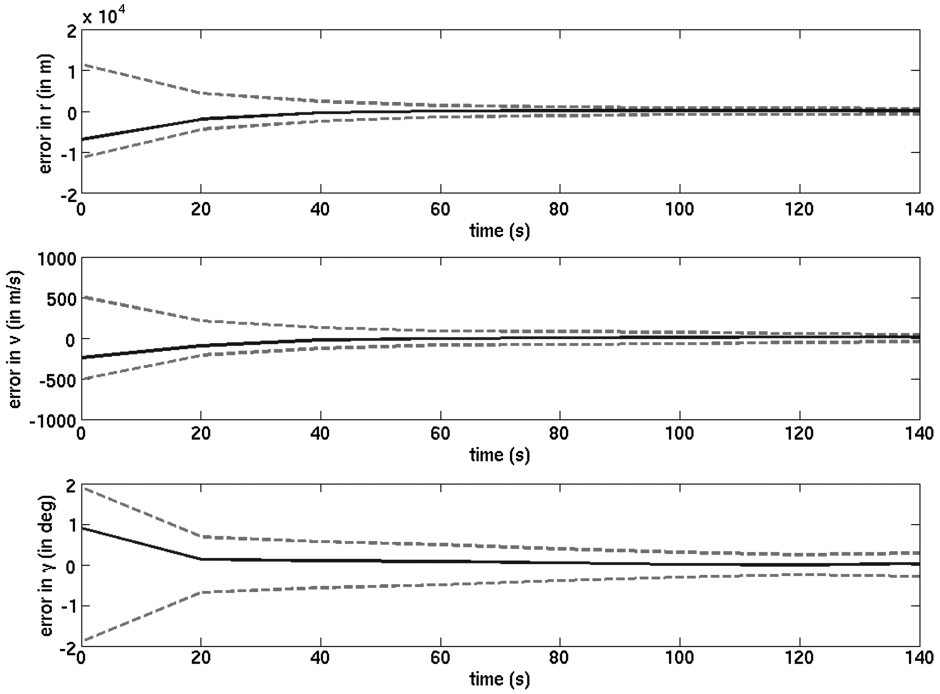

Fig. 4 Bootstrap filter. True initial states are $[R_m + 61\ \text{km},\ 2.64\ \text{km/s} - 8.1°]^T$, and the update interval is 20 s. The dashed lines represent $\pm 3\sigma$ limits, and the solid lines represent the error in estimation.

III. Uncertainty Propagation Using the Frobenius–Perron Operator

The problem of determining uncertainty in state due to parametric system uncertainty, for nonlinear systems, can be solved using the FP operator [25]. The definition of the operator in continuous time for the dynamical system

$$\dot{x} = f(x); \qquad x \in \mathcal{X} \subset \mathbb{R}^n, \qquad f{:}\mathcal{X} \mapsto \mathcal{X} \tag{2}$$

is given by the Liouville equation [25]:

$$\frac{\partial p}{\partial t} + \sum_{i=1}^{n} \frac{\partial [p f_i(x)]}{\partial x_i} = 0 \tag{3}$$

where $f(x) = [f_1(x) \cdots f_n(x)]^T$ and $p(t, x) := P_t p(t_0, x)$. The symbol P_t represents the continuous time FP operator, and $p(t_0, x)$ is the density function at initial time $t = t_0 \geq 0$.

The FP operator is a Markov operator and has the following properties [25]:

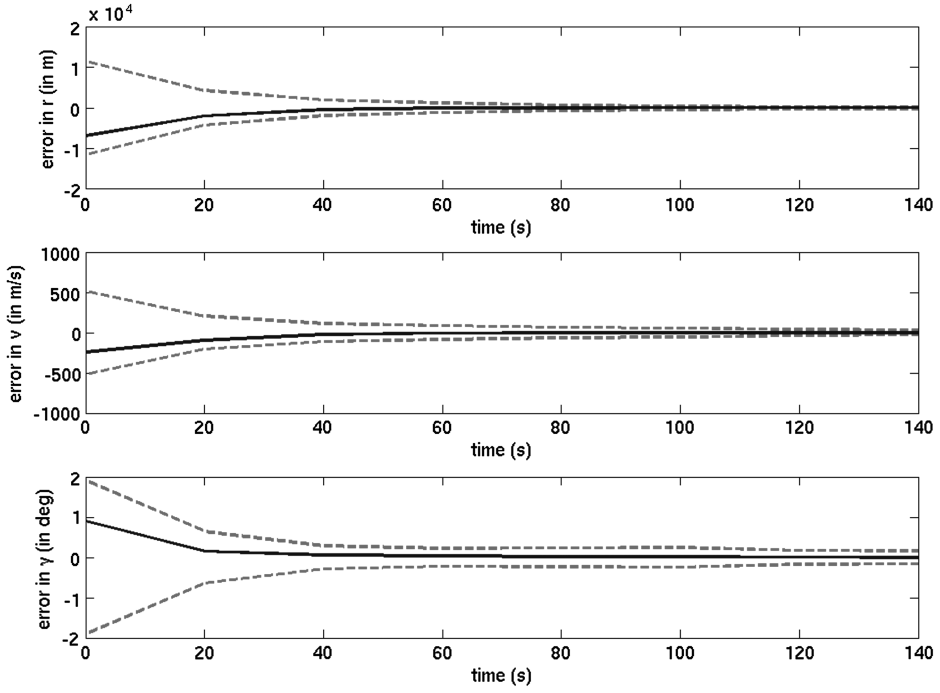

Fig. 5 Performance of the FP estimator with the true initial states as $[R_m + 61\ \text{km},\ 2.64\ \text{km/s} - 8.1°]^T$ and an update interval of 20 s. The dashed lines represent $\pm 3\sigma$ limits, and the solid lines represent the error in estimation.

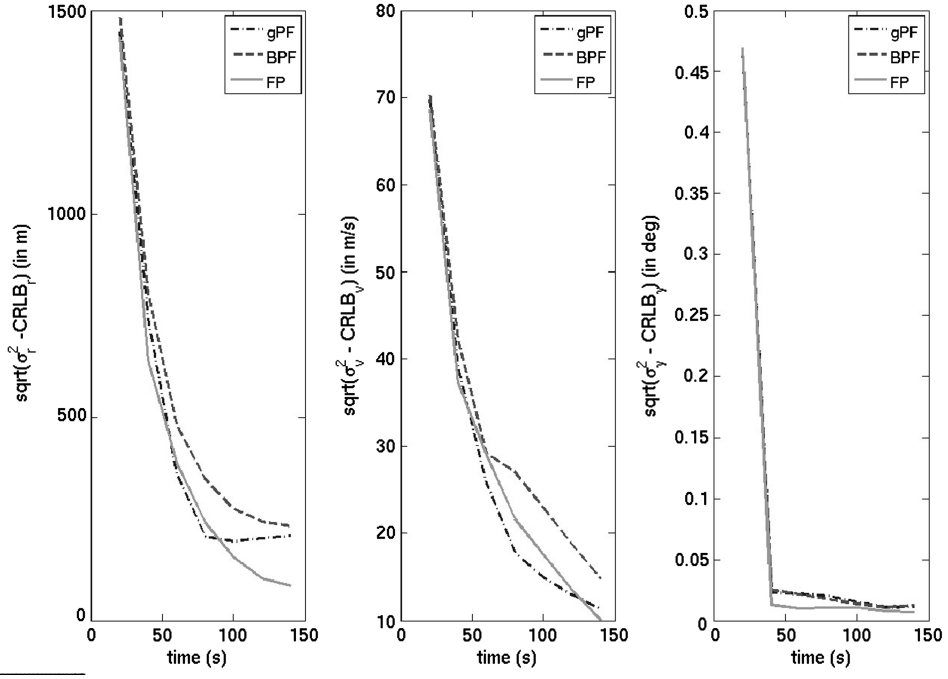

Fig. 6 Plots for $\sqrt{\sigma^2 - \mathrm{CRLB}}$ vs time for a) case I and b) case II. In the legend, BPF, gPF, and FP represent the bootstrap filter, the generic particle filter, and the FP operator-based estimator, respectively. (CRLB denotes Cramer–Rao lower bounds.)

1) Continuous

$$\lim_{t \to t_0} \| P_t p(t_0, x) - p(t_0, x) \| = 0$$

2) Linear

$$P_t[\lambda_1 p_1(t_0, x) + \lambda_2 p_2(t_0, x)] = \lambda_1 P_t p_1(t_0, x) + \lambda_2 P_t p_2(t_0, x)$$

such that $p_1(t_0, x)$, $p_2(t_0, x) \in \mathcal{L}^1$, λ_1, and $\lambda_2 \in \mathbb{R}$.

3) Positivity $P_t p(t_0, x) \geq 0$, if $p(t_0, x) \geq 0$.

4) Norm preserving

$$\int_{\mathcal{X}} P_t p(t_0, x) \mu\,(\mathrm{d}x) = \int_{\mathcal{X}} p(t_0, x) \mu\,(\mathrm{d}x)$$

such that $p(t_0, x) \in \mathcal{L}^1$, where $\mathcal{L}^1$ is a set of functions f: $\mathcal{X} \mapsto \mathbb{R}$ satisfying

$$\int_{\mathcal{X}} |f(x)| \mu\,(\mathrm{d}x) < \infty$$

and $\mu(\cdot)$ is a measure defined on $\mathcal{X}$. These properties ensure that the initial PDF $p(t_0, x)$ evolves continuously over time while satisfying properties of PDFs. Rigorous derivation of these and some of the

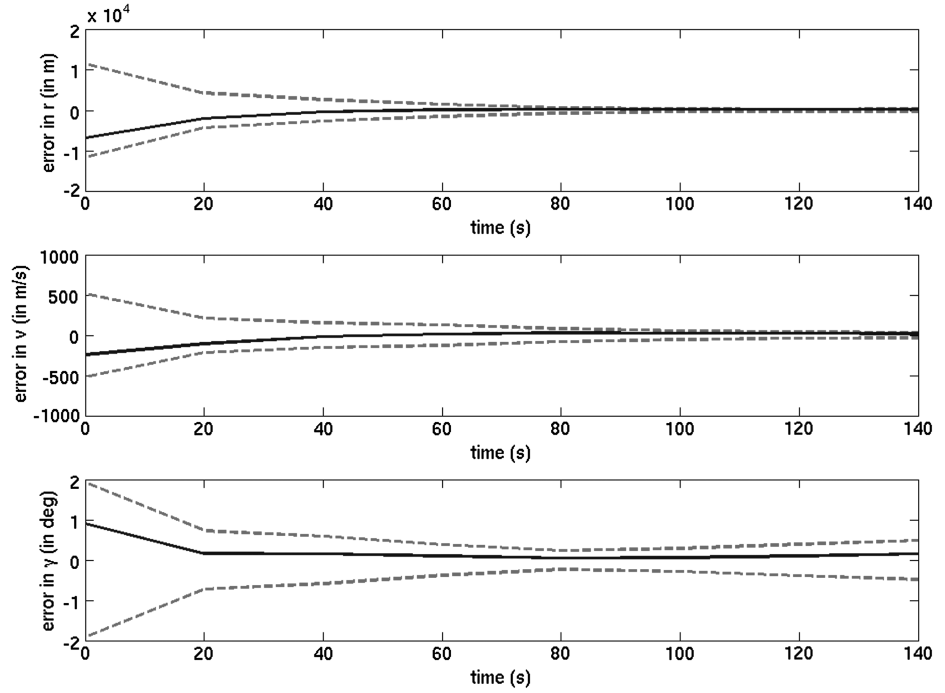

Fig. 7 Generic particle filter with 7000 samples. The true initial states are $[R_m + 61\ \mathrm{km},\ 2.64\ \mathrm{km/s} - 8.1°]^T$, and the update interval is 20 s. The dashed lines represent $\pm 3\sigma$ limits, and the solid lines represent the error in estimation.

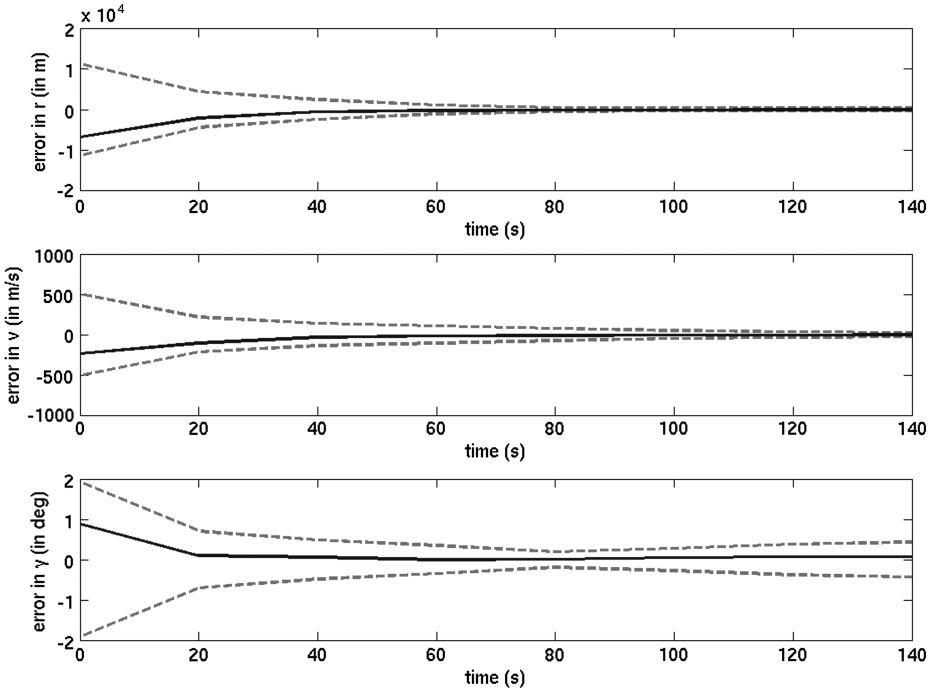

Fig. 8 Bootstrap filter with 7000 samples. The true initial states are $[R_m + 61\ \text{km},\ 2.64\ \text{km/s} - 8.1°]^T$, and the update interval is 20 s. The dashed lines represent $\pm 3\sigma$ limits, and the solid lines represent the error in estimation.

other properties of the FP operator has been omitted here and can be found in Lasota and Mackey [25].

A. Method of Characteristics for Solving First-Order Partial Differential Equations

Equation (3) is a first-order linear partial differential equation (PDE) that can be easily solved using the method of characteristics. Equation (3) can be written as

$$\frac{\partial p}{\partial t} + \frac{\partial p}{\partial x_1} f_1(x) + \cdots \frac{\partial p}{\partial x_n} f_n(x) + p \sum_{i=1}^{n} \frac{\partial f_i(x)}{\partial x_i} = 0$$

Defining

$$g(x, p) := -p \sum_{i=1}^{n} \frac{\partial f_i(x)}{\partial x_i}$$

we get

$$\frac{\partial p}{\partial t} + \frac{\partial p}{\partial x_1} f_1(x) + \cdots \frac{\partial p}{\partial x_n} f_n(x) = g(x, p) \tag{4}$$

which is in the standard form. Assuming $g(x, p) \neq 0$, Eq. (4) can be solved by solving $(n + 1)$ coupled ordinary differential equations given by

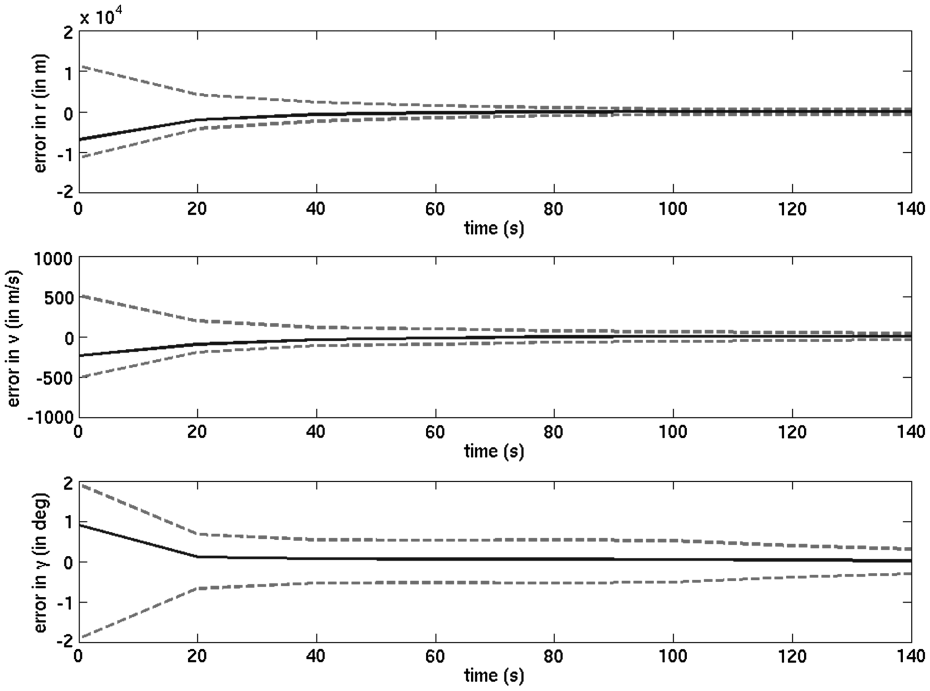

Fig. 9 Generic particle filter with 10,000 samples. The true initial states are $[R_m + 61\ \text{km},\ 2.64\ \text{km/s} - 8.1°]^T$, and the update interval is 20 s. The dashed lines represent $\pm 3\sigma$ limits, and the solid lines represent the error in estimation.

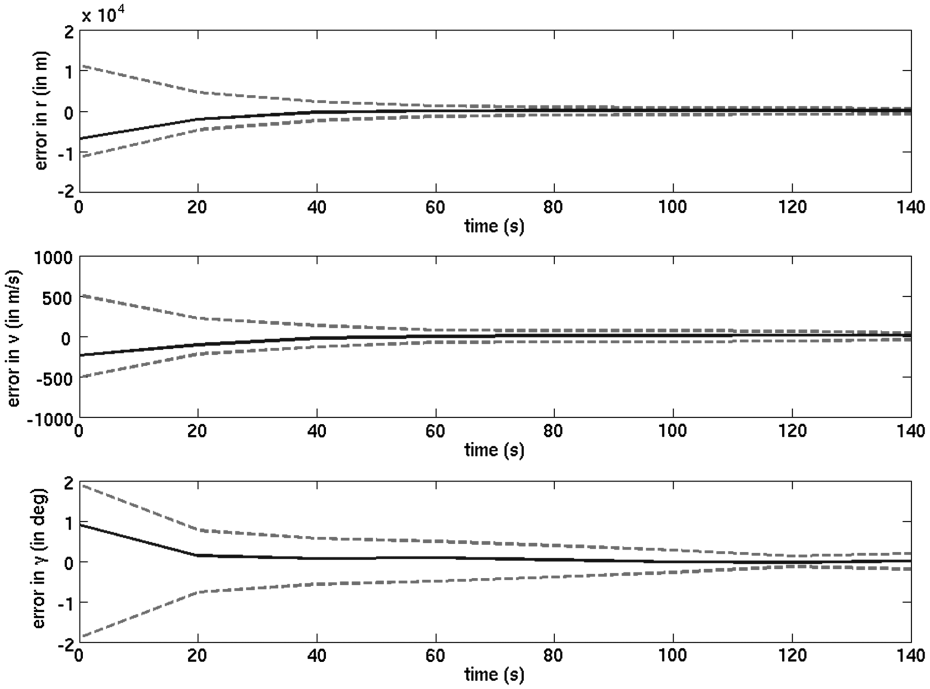

Fig. 10 Bootstrap filter with 10,000 samples. The true initial states are $[R_m + 61\ \text{km},\ 2.64\ \text{km/s} - 8.1°]^T$, and the update interval is 20 s. The dashed lines represent $\pm 3\sigma$ limits, and the solid lines represent the error in estimation.

$$\frac{\mathrm{d}x_1}{\mathrm{d}t} = f_1(x), \qquad \cdots, \qquad \frac{\mathrm{d}x_n}{\mathrm{d}t} = f_n(x), \qquad \frac{\mathrm{d}p}{\mathrm{d}t} = g(x, p) \quad (5)$$

These equations trace out a trajectory in the $(n + 1)$ dimensional space spanned by $(x_1, \cdots, x_n, p)$. To make the solution unique, the value of $p(t, x)$ has to be specified at a given point $x(t_0)$ at time t_0. The evolution of $p(t, x)$ over $\mathbb{R} \times \mathcal{X}$ can be determined by specifying $p(t, x)$ over several points in $\mathcal{X}$ at time t_0. These points are obtained by sampling the density function at t_0. The trajectories $x(t)$ are called characteristics, and Eq. (5) determines the evolution of p along $x(t)$. For additional details, the reader is directed to [34].

For example, consider uncertainty propagation due to initial condition uncertainty for the Duffing oscillator model. As shown in Fig. 1, consider the case where there is an initial condition about $(1, 1)$. The distribution is considered to be Gaussian. The initial distribution is sampled using 500 points. The corresponding differential equation for uncertainty propagation is

$$\dot{x}_1 = x_2 \quad (6)$$

$$\dot{x}_2 = x_1 - x_1^3 - x_2 \quad (7)$$

$$\dot{p} = -p(0 + -1) = p \quad (8)$$

The initial conditions for (x_1, x_2) are given by the locations of the samples. The initial conditions for p are given by the values of the Gaussian distribution function at those points. With these initial conditions, the preceding equations are integrated to obtain $[x_1(t), x_2(t), p(t)]$. Figure 1 shows the initial values of

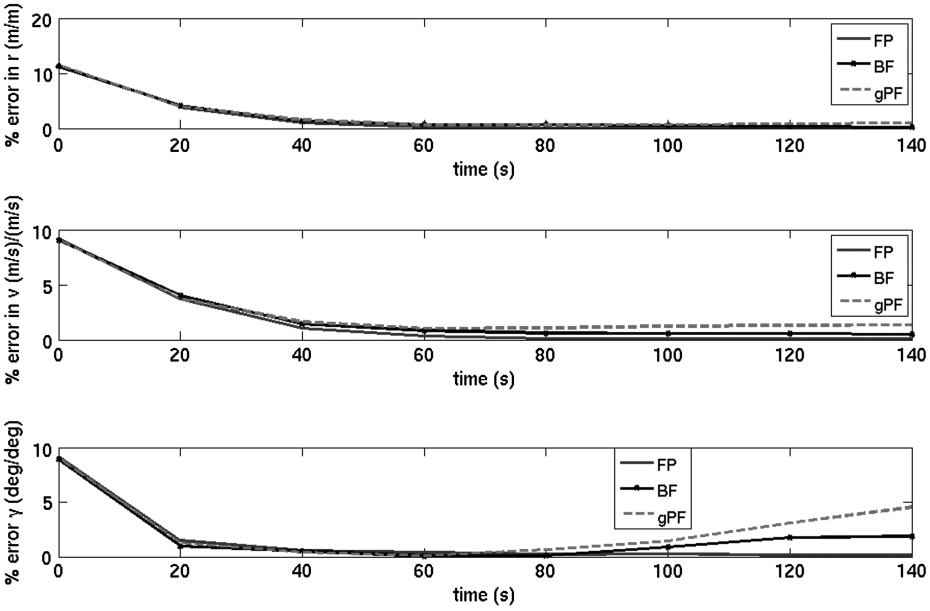

Fig. 11 Percentage error in estimation with 7000 samples. The true initial states are $[R_m + 61\ \text{km},\ 2.64\ \text{km/s} - 8.1°]^T$, and the update interval is 20 s. In the legend, BF, gPF, and FP represent the bootstrap filter, the generic particle filter, and the FP operator-based estimator, respectively.

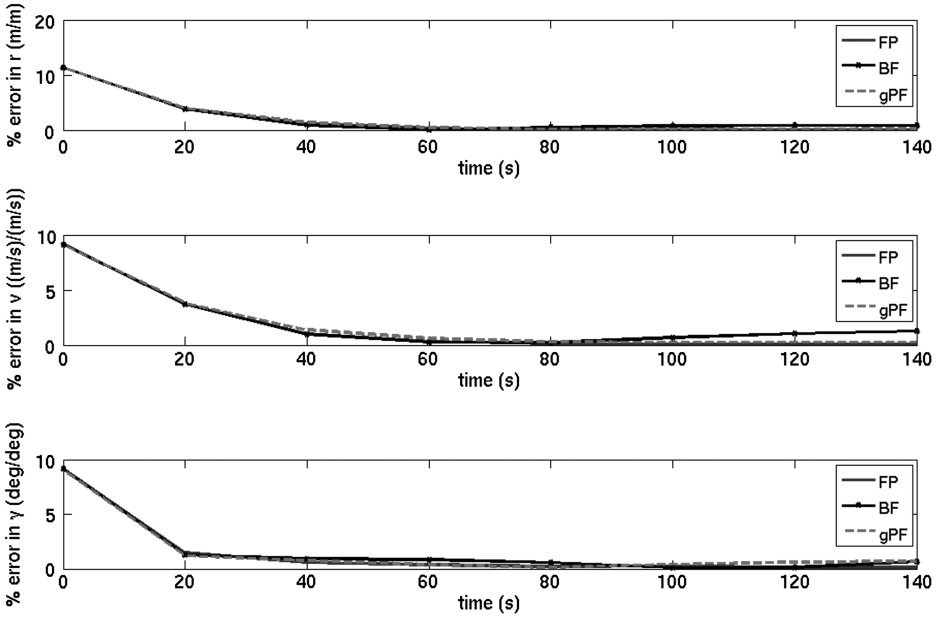

Fig. 12 Percentage error in estimation with the number of samples for the FP-based operator (FP), the generic particle filter (gPF), and the bootstrap filter (BF) as 7,000, 20,000, and 25,000, respectively. The true initial states are $[R_m + 61\ \text{km}\ 2.64\ \text{km/s} - 8.1°]^T$, and the update interval is 20 s.

$[x_1(t), x_2(t), p(t)]$ and their values at time $t = 1$ s. It can be observed that this method determines the value of p at (x_1, x_2) exactly. For intermediate points, interpolation will have to be used. Also note that the value of p determined at (x_1, x_2) at some time t is independent of the number of samples, although increasing the number of samples will improve the accuracy of the subsequent interpolation. However, in the case of particle filtering, since the value of p is approximated using histograms, the accuracy depends on the number of samples.

B. Accuracy in Prediction of Uncertainty

Since this method requires a selection of points in the state space, one may argue that this approach is similar to MC. The main difference is that, in the FP operator, the value of the density function is determined along the trajectory, and at a final time, the value of the density function is known at certain discrete locations. These locations are values of the state vector at that final time. The value of the density function over the domain is then determined using interpolation. In MC, the same idea is used, except only state equations are integrated. The density function at the final time is determined using histogram techniques, which are sensitive to the number of sample points taken. Thus, for comparable accuracy, many more points will have to be taken for the MC-based method than for the FP-based method. As an illustration, consider Fig. 2. It can be seen that a good approximation of the Gaussian density function is achieved by taking 25 points and linear interpolation in the case of FP operators, whereas for MC, at least 1000 points were needed to get the same level of accuracy. Thus, for this one-dimensional case, there is a reduction of two orders of magnitude in the number of sample points required for FP-based uncertainty propagation. For a higher-dimensional case, the benefits will be even more significant. For high-dimensional problems, discrete points can be generated using the Halton sequence [35], and concentrating them in regions with higher importance/features will further reduce the growth of computational complexity. Other methods for generating smart samples from a given distribution include sparse grids [36–38] and mesh-free adjoint methods [31,39–41].

IV. Nonlinear Estimation Using the Frobenius–Perron Operator

Let the dynamical system and measurement model be given by Eq. (1). It is assumed that measurements are available at discrete times $t_0, \cdots, t_{k-1}, t_k, t_{k+1}, \cdots$. At a given time t_k, let x_k, y_k, and $p_k(\cdot)$ be the state, measurement, and PDF. Let $p_k^-(\cdot)$ and $p_k^+(\cdot)$ denote the prior and the posterior density functions at time t_k. The estimation algorithm is described next, which is similar to that presented by Daum and Krichman [30].

A. Step 1: Initialization Step

To begin, the domain $\mathcal{D}_\Delta$ of the initial random variable x_0 is discretized. From the discretized domain, N samples are chosen at random based on the PDF $p_0(x_0)$ of the random variable x_0. Let the samples be represented by $x_{0,i}$ for $i = 1, 2, \cdots, N$ and $p_0(x_{0,i})$ be the value of $p_0(x)$ at these sample points. The following steps are then performed recursively, starting from $k = 1$.

B. Step 2: Propagation Step

With the initial states at the $k-1$th step as $[x_{k-1,i} p_{k-1}(x_{k-1,i})]^T$, Eq. (5) is integrated for each grid point over the interval $[t_{k-1}, t_k]$ to get $[x_{k,i}, p_k^-(x_{k,i})]^T$. Note that $p_k(x_{k,i})$, obtained by integration, are the prior PDF values for $x_{k,i}$, and hence the superscript.

C. Step 3: Update Step

First, the likelihood function, $p(\tilde{y}_k | x_k = x_{k,i})$, is determined for each grid point i using Gaussian measurement noise and the sensor model in Eq. (1b). It is defined as

$$l(\tilde{y}_k | x_k = x_{k,i}) = \frac{1}{\sqrt{(2\pi)^m |R|}} e^{-(1/2)[\tilde{y}_k - h(x_{k,i})]^T R^{-1} [\tilde{y}_k - h(x_{k,i})]}$$

where $|R|$ is the determinant of the covariance matrix of measurement noise.

The posterior PDF of the states is constructed next for each grid point i using classical Bayes rule [42]. It is defined as the density function of the states given current measurement: i.e., $p_k^+(x_{k,i}) := p_k(x_k = x_{k,i} | \tilde{y}_k)$. For a particular sample, $x_{k,i}$ is given by

$$p_k^+(x_{k,i}) := p(x_k = x_{k,i} | \tilde{y}_k) = \frac{l(\tilde{y}_k | x_k = x_{k,i}) p_k^-(x_k = x_{k,i})}{\sum_{j=1}^N l(\tilde{y}_k | x_k = x_{k,j}) p_k^-(x_k = x_{k,j})} \tag{9}$$

D. Step 4: Getting the State Estimate

The state estimate for the kth step is then computed, depending on the desired computation as given in Bryson and Ho [43]. The following are commonly used criteria.

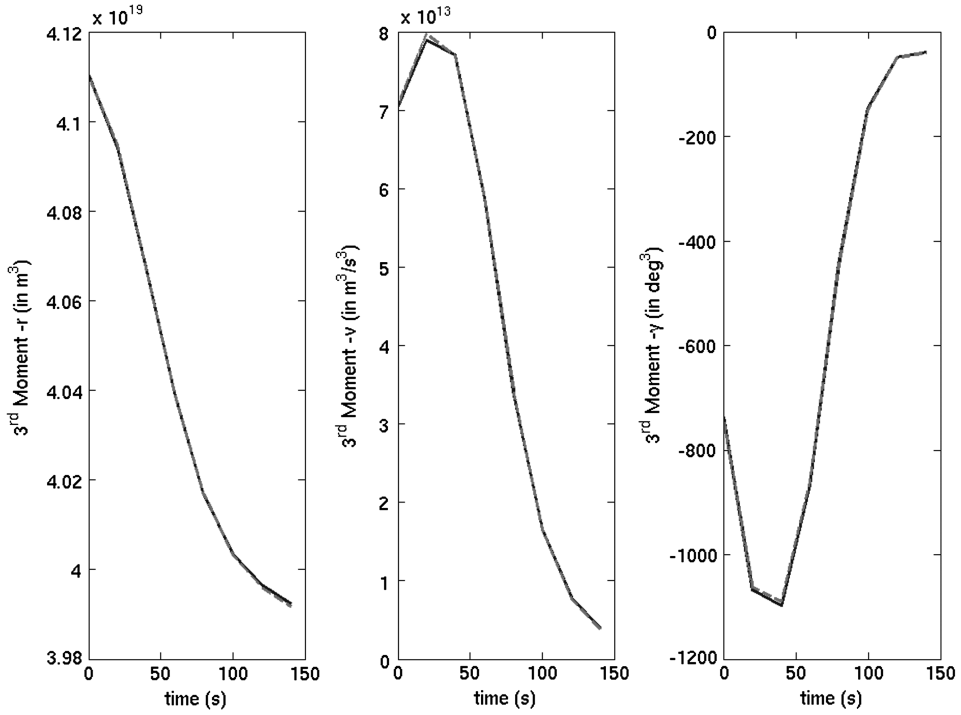

a) 3*rd* order moments

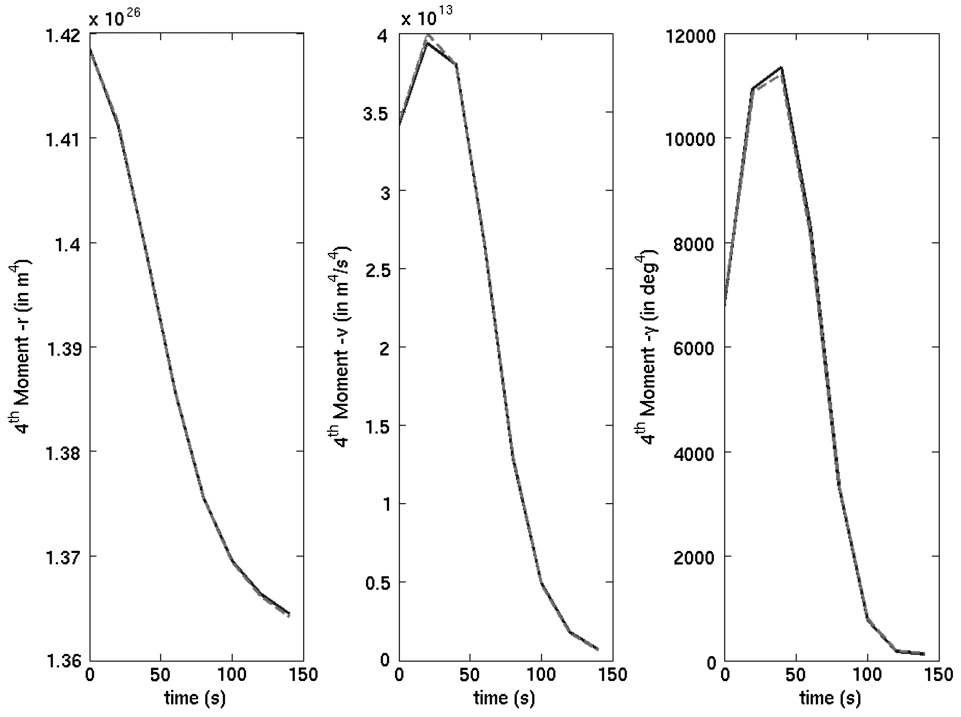

b) 4*th* order moments

Fig. 13 Plots for third- and fourth-order moments for the particle filter with 100,000 samples (dashed line) and the FP operator-based filter with 7000 samples (solid line).

1) For the maximum-likelihood estimate, maximize the probability that $x_{k,i} = \hat{x}_k$. This results in $\hat{x}_k =$ mode of $p_k^+(x_{k,i})$.

2) For the minimum-variance estimate,

$$\hat{x}_k = \arg\min_x \sum_{i=1}^{N} \|x - x_{k,i}\|^2 p_k^+(x_{k,i}) = \sum_{i=1}^{N} x_{k,i} p_k^+(x_{k,i})$$

The estimate is the mean of $x_{k,i}$.

3) For the minimum-error estimate, minimize maximum $|x - x_{k,i}|$. This results in $\hat{x} =$ median of $p_k^+(x_{k,i})$.

E. Step 5: Resampling

The degeneracy of sample points can be detected by looking at values of $x_{k,i}$ for which $p_k^+(x_{k,i}) < \epsilon$, where $\epsilon \ll 1$ and is prespecified. Existing methods for resampling can be used to generate new points from the new distribution $p_k^+(x_{k,i})$. For the $k+1$th step, new points and the corresponding posterior density $p_k^+(x_{k,i})$ serve as initial states. Qualitatively, since histogram techniques are not used in determining density functions, this method is less sensitive to the issue of degeneracy, although a rigorous analysis of this has not been done.

Table 4 Computational time taken per filtering step for each estimation algorithm

Filter	Computational time, s
FP operator-based filter	57.42
Generic particle filter	207.96
Bootstrap filter	168.06

V. Application to Hypersonic Reentry Problem

A. Application to Three-State Vinh's Equation

The estimation algorithm presented here is applied to the reentry of hypersonic vehicles. The simplified dynamics of reentry are represented by the Vinh's equation [44] in three states: the distance from the planet's center r, the velocity v, and the flight-path angle γ or $x = [\,r \quad v \quad \gamma\,]^T$. The equations can be written as

$$\dot{r} = v\sin(\gamma) \tag{10a}$$

$$\dot{v} = -\frac{\rho v^2}{2B_c} - g\sin(\gamma) \tag{10b}$$

$$\dot{\gamma} = \left(\frac{v}{r} - \frac{g}{v}\right)\cos(\gamma) + \frac{\rho}{2B_c}\left(\frac{L}{D}\right)v \tag{10c}$$

where g is the acceleration due to gravity, B_c is the ballistic coefficient, $\frac{L}{D}$ is the lift-to-drag ratio of the vehicle, and ρ is the atmospheric density given by

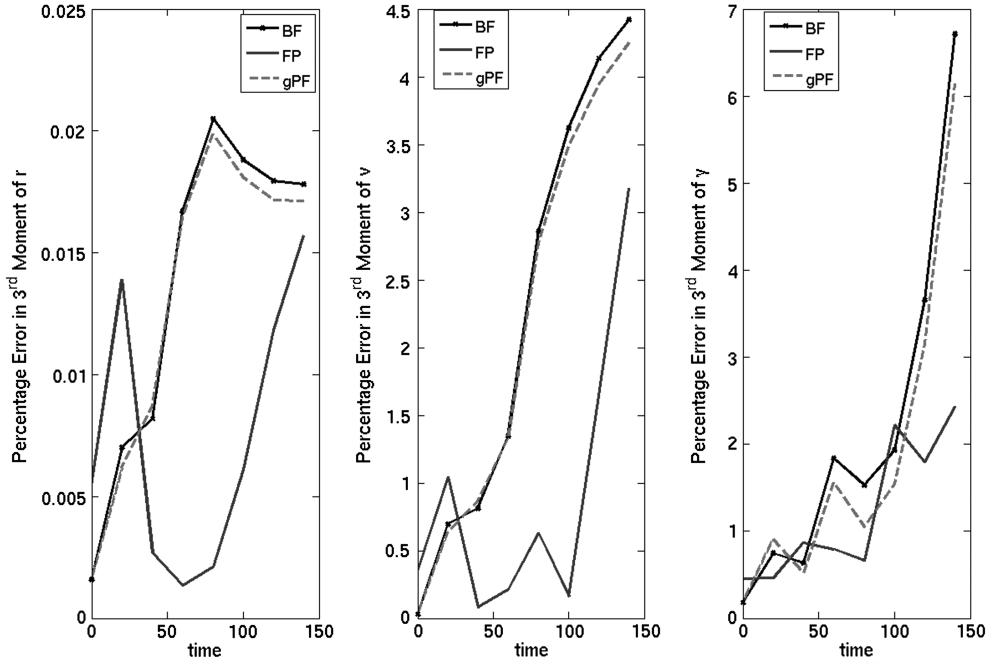

a) Percentage Error in 3rd order moments

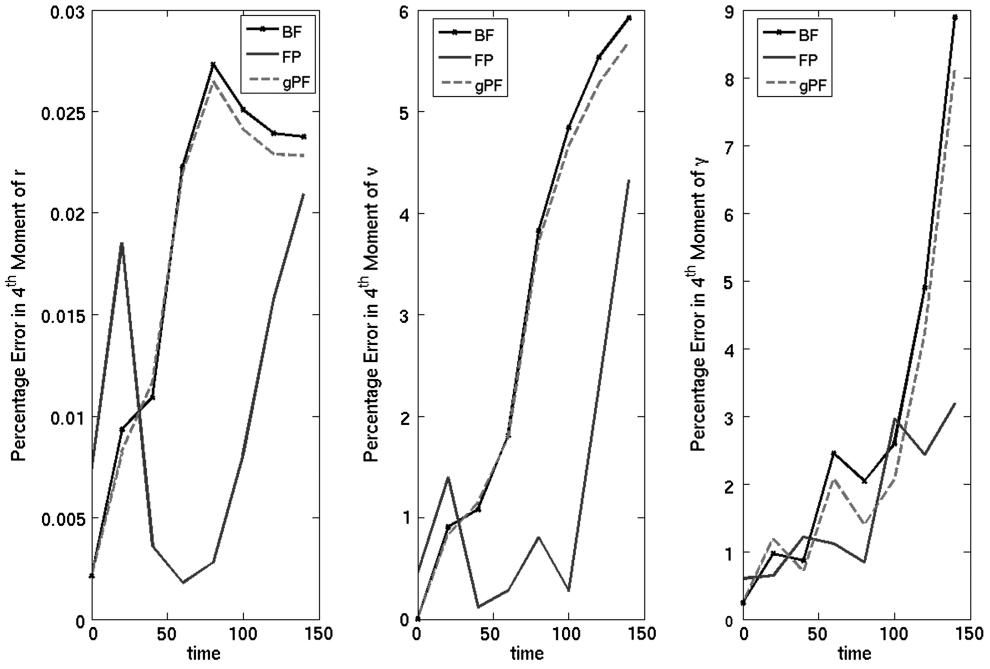

b) Percentage Error in 4th order moments

Fig. 14 Plots for percentage error in third- and fourth-order moments for the bootstrap filter (BF), the generic particle filter (gPF), and the FP operator-based filter (FP), all with 7000 samples. The percentage deviation was taken from the particle filter with 100,000 samples.

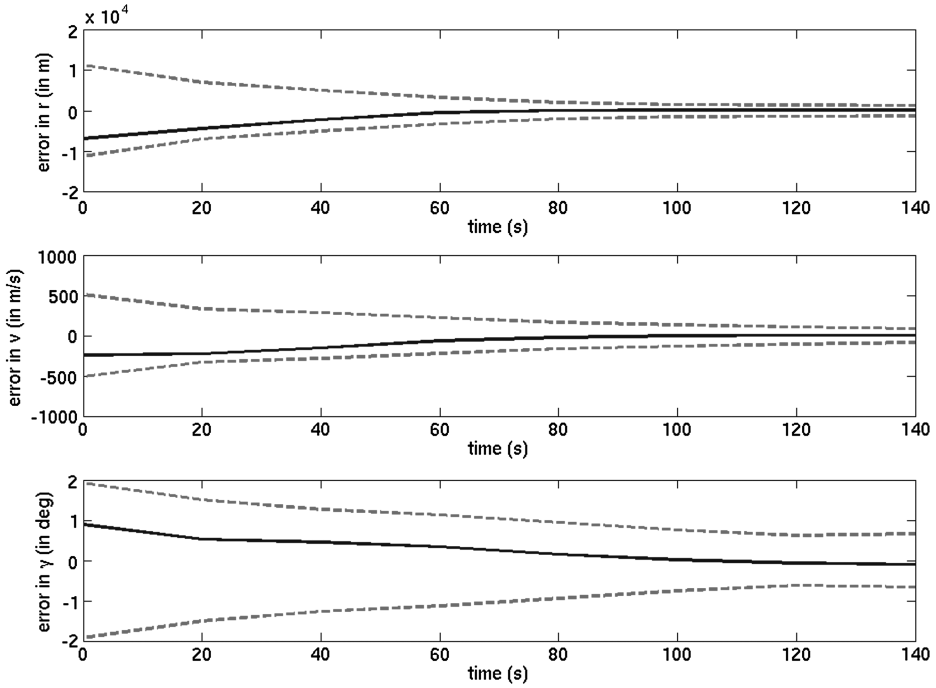

Fig. 15 FP operator-based filter with measurement noise $6 \times 10^{-4}\mathcal{I}_3$ in scaled units (number of samples = 7000). The true initial states are $[R_m + 61\ \text{km}\ 2.64\ \text{km/s} - 8.1°]^T$. The dashed lines represent $\pm 3\sigma$ limits, and the solid lines represent the error in estimation.

$$\rho = \rho_0 e^{[(h_2 - h)/h_1]} \qquad \bar{q} = \tfrac{1}{2}\rho v^2, \qquad Q = k\rho^{1/2} v^{3.15}, \qquad G = \gamma \tag{11}$$

where ρ_0, h_1, and h_2 are constants depending on the planet's atmospheric model, $h = r - R_m$ is the height above the planet's surface, and R_m is the radius of the planet. The choices of the constants in Eq. (10) used to simulate reentry in the Martian atmosphere are given in Table 1.

The measurement model $\tilde{y}$ consists of the dynamic pressure $\bar{q}$, the heating rate Q [45], and the flight-path angle or $\tilde{y} = [\,\bar{q} \quad Q \quad G\,]^T$, for which the expressions are

where $k = 4.47228 \times 10^{-9}$ is the scaled material heating coefficient.

Here, the initial state uncertainty with the Gaussian distribution has been considered; that is, $x(0, \Delta) = \Delta \sim \mathcal{N}(\mu_0, \sigma_0^2)$, where μ_0 and σ_0 are the mean and standard deviation, respectively, and have the values

$$\mu_0 = [R_m + 54\ \text{km}, 2.4\ \text{km/s}, -9°]^T \tag{12a}$$

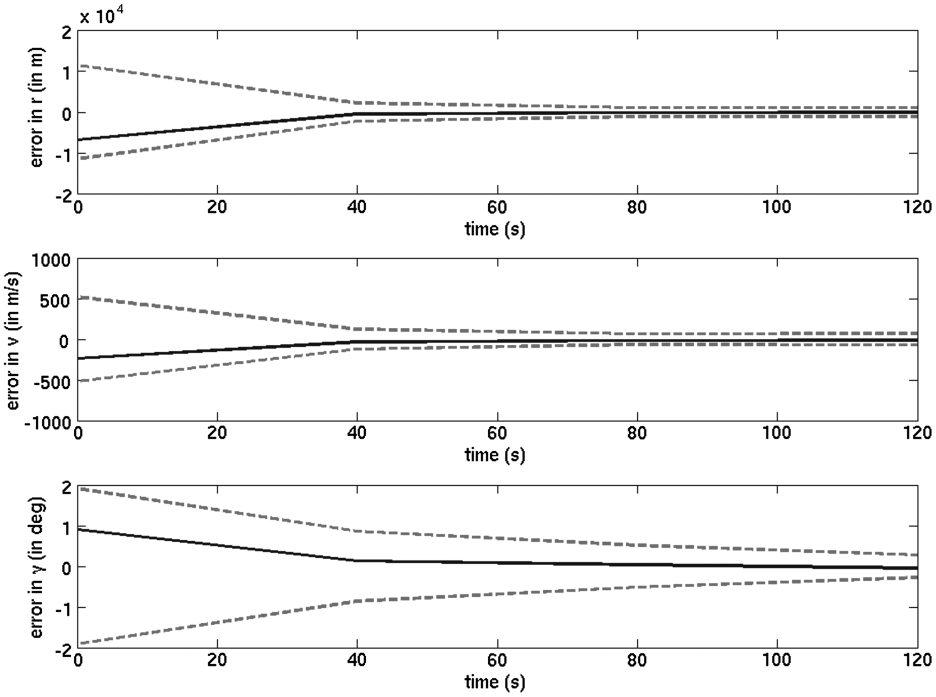

Fig. 16 FP operator-based filter measurement update interval in 40 s (number of samples = 7000). The true initial states are $[R_m + 61\ \text{km},\ 2.64\ \text{km/s} - 8.1°]^T$. The dashed lines represent $\pm 3\sigma$ limits, and the solid lines represent the error in estimation.

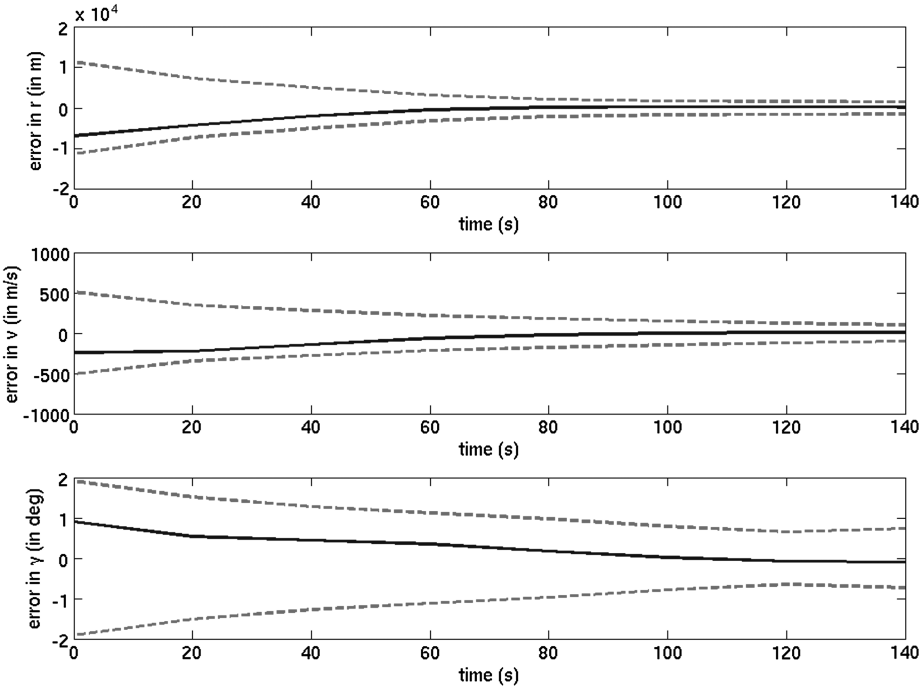

Fig. 17 Generic particle filter with measurement noise $6 \times 10^{-4}\mathcal{I}_3$ in scaled units (number of samples = 25,000). The true initial states are $[R_m + 61\ \text{km},\ 2.64\ \text{km/s} - 8.1°]^T$. The dashed lines represent $\pm 3\sigma$ limits, and the solid lines represent the error in estimation.

$$\sigma_0 = \begin{pmatrix} 5.4\ \text{km} & 0 & 0 \\ 0 & 240\ \text{m/s} & 0 \\ 0 & 0 & 0.9° \end{pmatrix} \tag{12b}$$

To achieve consistency in dimensions, every constant in Eq. (10) is appropriately scaled to create a nondimensionalized system. The constants scaling the base units are given in Table 2.

The measurements are normalized to lie within $[-1, 1]$, so that they have consistent magnitude. The normalization factors used for measurements are given in Table 3. The measurement noise ν is assumed to have mean and covariance, $\mathbf{E}[\nu] = [0, 0, 0]^T$ and $R = \mathbf{E}[\nu\nu^T] = 6 \times 10^{-5}\mathcal{I}_3$, respectively, in scaled units.

The performance of the FP operator-based nonlinear estimator is now compared with the generic particle filter and the bootstrap filter when applied to hypersonic reentry dynamics. The initial states of the actual system are taken as $[R_m + 61\ \text{km},\ 2.64\ \text{km/s} - 8.1°]^T$ in this case, with v and γ having 10% errors in the state estimate. The measurement update rate was taken to be 20 s. Figures 3–5 show the plots for the particle filter, the bootstrap filter, and the FP filter, respectively. Figure 6 shows the Cramér–Rao bounds for the three filters. From these plots, it can be seen that all three filters perform equally well and the errors are within the $\pm 3\sigma$ limits. The number of samples used in these simulations for the particle filter, the bootstrap filter, and the FP filter are 25,000, 20,000, and 7,000, respectively.

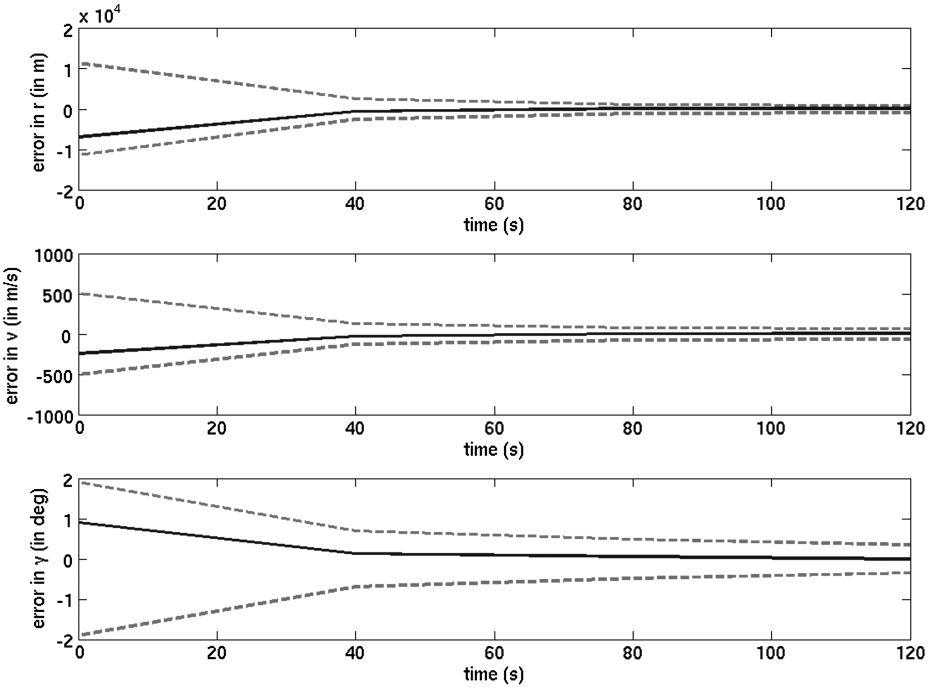

Fig. 18 Generic particle filter measurement update interval in 40 s (number of samples = 25,000). The true initial states are $[R_m + 61\ \text{km},\ 2.64\ \text{km/s} - 8.1°]^T$. The dashed lines represent $\pm 3\sigma$ limits, and the solid lines represent the error in estimation.

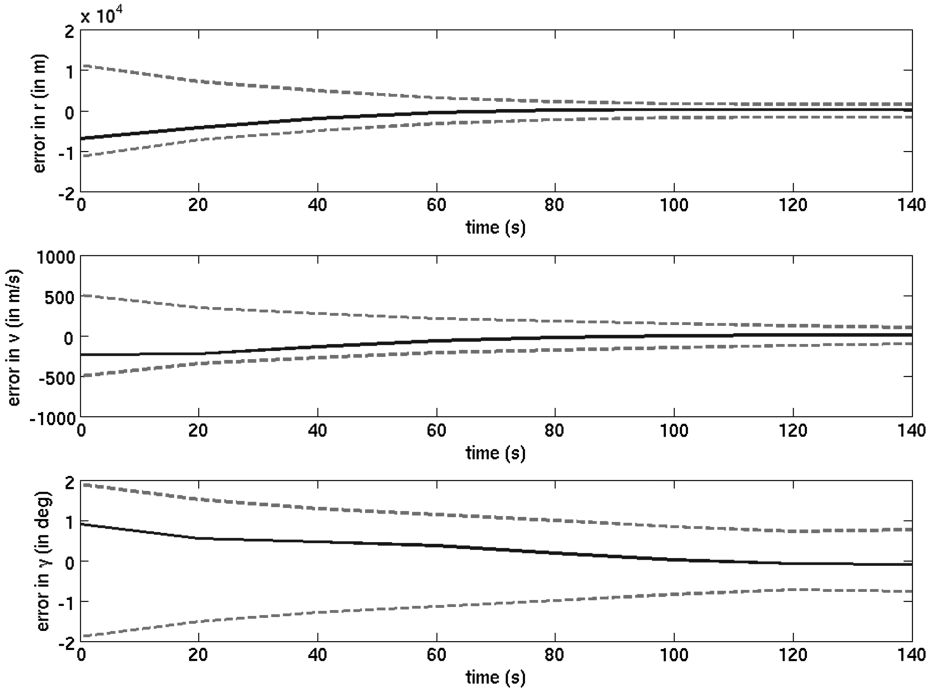

Fig. 19 Bootstrap filter with measurement noise $6 \times 10^{-4}\mathcal{I}_3$ in scaled units (number of samples = 20, 000). The true initial states are $[R_m + 61\ \text{km},\ 2.64\ \text{km/s} - 8.1°]^T$. The dashed lines represent $\pm 3\sigma$ limits, and the solid lines represent the error in estimation.

The particle and bootstraps filter did not perform as well as the FP filter with the lesser number of samples. Figures 7 and 8 show plots for error covariance and estimation errors for the generic particle filter and the bootstrap filter, respectively. It can bee seen that they do not perform as well as the FP operator-based estimator (Fig. 5). In Figs. 9 and 10, the number of samples were increased to 10,000 for the particle-filter-based estimators. Even then, the performance of the particle filters do not match with the FP operator-based estimator's performance. To substantiate our claim, the percentage error vs the time of the three estimators has been compared here. Figure 11 show plots when the number of samples for each estimator is fixed at 7000. It can be seen that the percentage error in the state estimate for the FP operator-based estimator is lower than the particle-filter-based estimators. The performance of the particle filters matches the FP operator only when the number of samples for the generic particle filter is 25,000 and the number of samples for the bootstrap filter is 20,000; the percentage error plots for these are shown in Fig. 12.

Thus, it can be said that the FP filter can achieve the same result as particle filters using a significantly lower number of samples. These simulations were performed in a Linux machine with an Intel® Pentium D processor. The superiority of the FP filter is in the computational time. For each filtering algorithm, the computational time taken for one filtering step is presented in Table 4. It can be seen

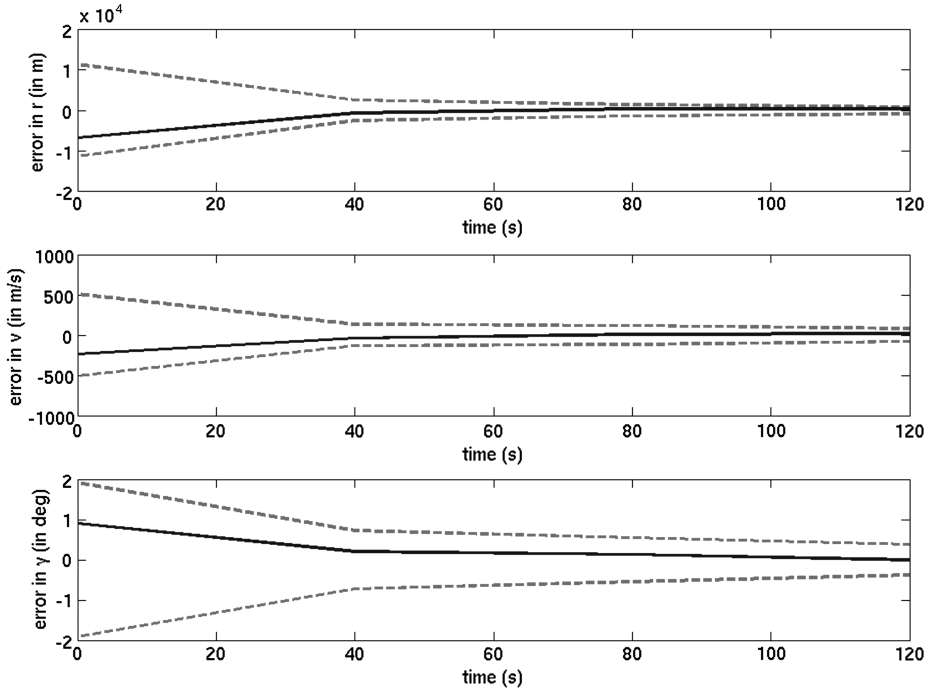

Fig. 20 Bootstrap filter measurement update interval in 40 s (number of samples = 20, 000). The true initial states are $[R_m + 61\ \text{km},\ 2.64\ \text{km/s} - 8.1°]^T$. The dashed lines represent $\pm 3\sigma$ limits, and the solid lines represent the error in estimation.

that, due to a fewer number of samples, the FP filter takes significantly less computational time.

The FP operator-based estimator captures the non-Gaussian PDF evolution almost accurately. To show this, time evolution of the third and fourth moments of the posterior PDF for the FP operator-based estimator with 7000 samples and a particle filter with a large number of samples (100,000) has been plotted in Fig. 13. It can be seen that the moments for the FP operator match exactly with the particle filter. If the generic particle filter and the bootstrap filter with 7000 samples are compared, it is observed that they fail to predict non-Gaussian PDF evolution as accurately as the FP operator-based estimator. To show this percentage deviation of the third- and fourth-order moments of the three estimators, the particle filter with 100,000 samples has been plotted in Fig. 14. It can be seen that the percentage error for the FP operator-based estimator is lower than the particle-filter-based estimators.

Table 5 Normalization factors used for measurements

Measurement	Normalization factors
Dynamic pressure	1.97×10^3 N/m
Heating rate	0.0231 J/m · s
Flight-path angle	19.13°
Geocentric longitude	60.6°
Geocentric latitude	30.3°

Regarding sensitivity with respect to measurement noise and the measurement update rate, Figs. 15 and 16 show plots of the error

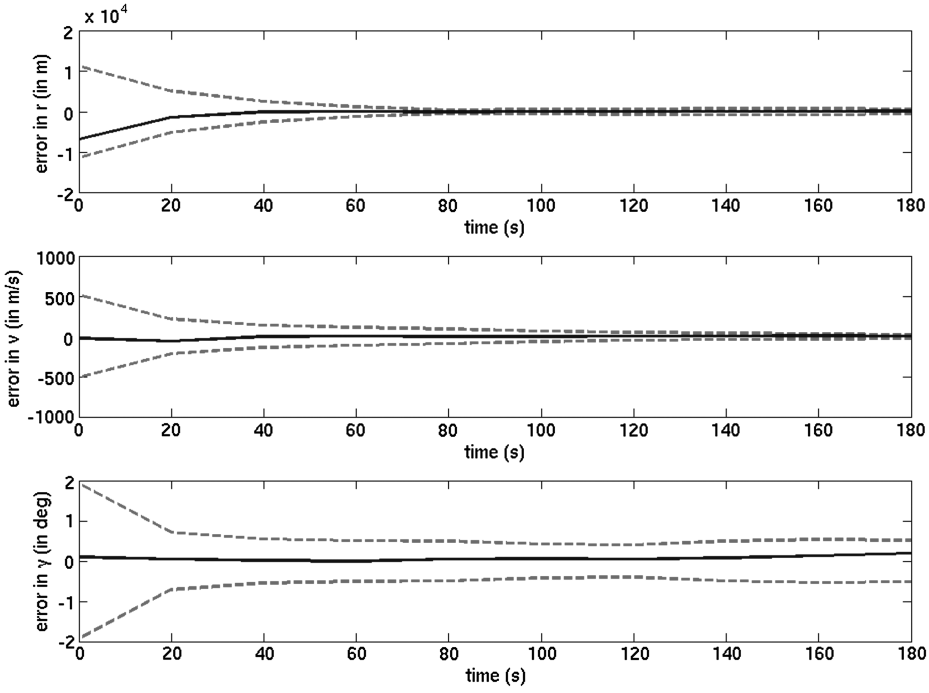

a) Plots for r, υ and γ

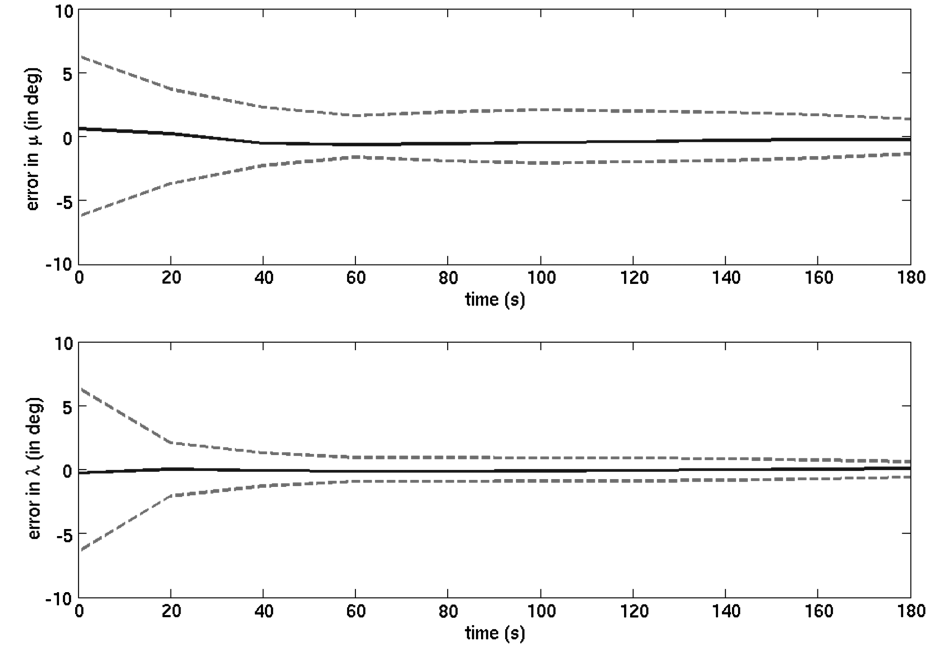

b) Plots for θ and λ

Fig. 21 Performance of FP operator-based filter with 9000 samples, when applied to the six-state Vinh's equation. The dashed lines represent $\pm 3\sigma$ limits, and the solid lines represent the error in estimation.

covariance and the state estimate error for the FP operator-based filter when the measurement noise is $6 \times 10^{-4}\mathcal{I}_3$, in scaled units, and when the measurement update rate is 40 s, respectively. The number of samples taken here is 7000. To achieve a similar performance, the generic particle filter and the bootstrap filter needed 20,000 and 25,000 samples, respectively. The plots for the particle filter are shown in Figs. 17 and 18, and the plots for the bootstrap filter are shown in Figs. 19 and 20.

B. Application to Six-State Vinh's Equation

The estimation algorithm presented is then applied to reentry of a hypersonic vehicle in Mars' atmosphere, with dynamics governed by the six-state Vinh's equation [45]. The equations of motion are given by

$$\dot{r} = v\sin\gamma \tag{13a}$$

$$\dot{\theta} = \frac{v\cos\gamma\cos\xi}{r\cos\lambda} \tag{13b}$$

$$\dot{\lambda} = \frac{v\cos\gamma\sin\xi}{r} \tag{13c}$$

$$\dot{v} = -\frac{\rho v^2}{2B_c} - g\sin\gamma - \Omega^2 r\cos\lambda(\sin\gamma\cos\lambda - \cos\gamma\sin\lambda\sin\xi) \tag{13d}$$

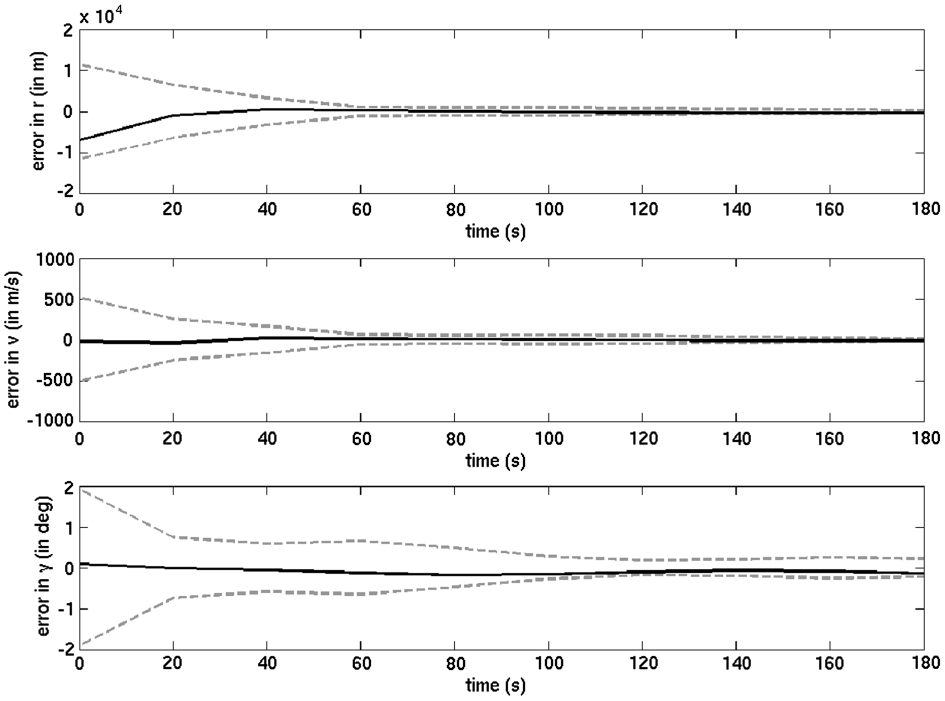

a) Plots for r, v and γ

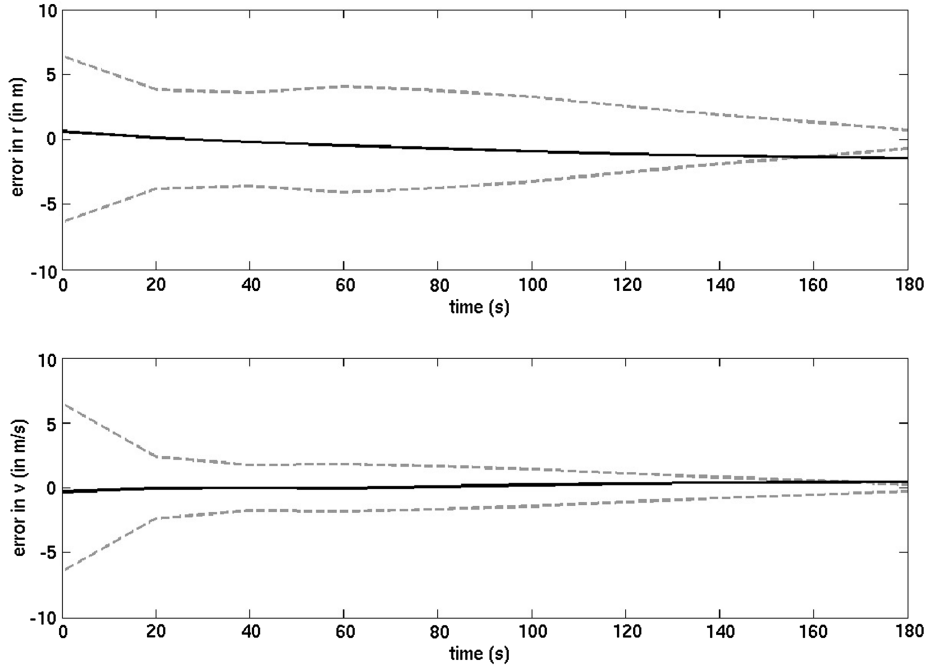

b) Plots for θ and λ

Fig. 22 Performance of generic particle filter with 9000 samples when applied to the six-state Vinh's equation. The dashed lines represent $\pm 3\sigma$ limits, and the solid lines represent the error in estimation.

$$\dot{\gamma} = \left(\frac{v}{r} - \frac{g}{v}\right)\cos(\gamma) + \frac{\rho}{2B_c}\left(\frac{L}{D}\right)v\cos\sigma + 2\Omega\cos\lambda\cos\xi + \frac{\Omega^2 r}{v}\cos\lambda(\cos\gamma\cos\lambda + \sin\gamma\sin\lambda\sin\xi) \quad (13e)$$

$$\dot{\xi} = \frac{\rho}{2B_c}\left(\frac{L}{D}\right)v\sin\sigma - \frac{v}{r}\cos\gamma\cos\xi\tan\lambda + 2\Omega(\tan\gamma\cos\lambda\sin\xi - \sin\lambda) - \frac{\Omega^2 r}{v\cos\gamma}\sin\lambda\cos\lambda\cos\xi \quad (13f)$$

where θ is the geocentric longitude, λ is the geocentric latitude, and ξ is the hypersonic vehicle's heading angle. Ω is the angular velocity of Mars given by 7.0882×10^{-5} rad/s, and σ is the bank angle, which is taken as 0° in this case.

The measurement model $\tilde{y}$ consists of measurements of geocentric latitude and longitude, θ and λ, along with dynamic pressure $\bar{q}$, heating rate Q, and flight-path angle γ, for which the expressions are given in Eq. (11). Hence, the measurement model is given by $\tilde{y} = [\bar{q} \quad Q \quad G \quad \theta \quad \lambda]^T$.

The vehicle's heading angle ξ is assumed to have no initial state uncertainty, and it has an initial value of 0.0573°. The Gaussian initial condition uncertainty, along r, θ, λ, v, and γ, is considered, with the mean μ_0 and standard deviation σ_0 given by

$$\mu_0 = [R_m + 54 \text{ km}, \ -60°, \ 30°, \ 2.4 \text{ km/s}, \ -9°]^T \quad (14a)$$

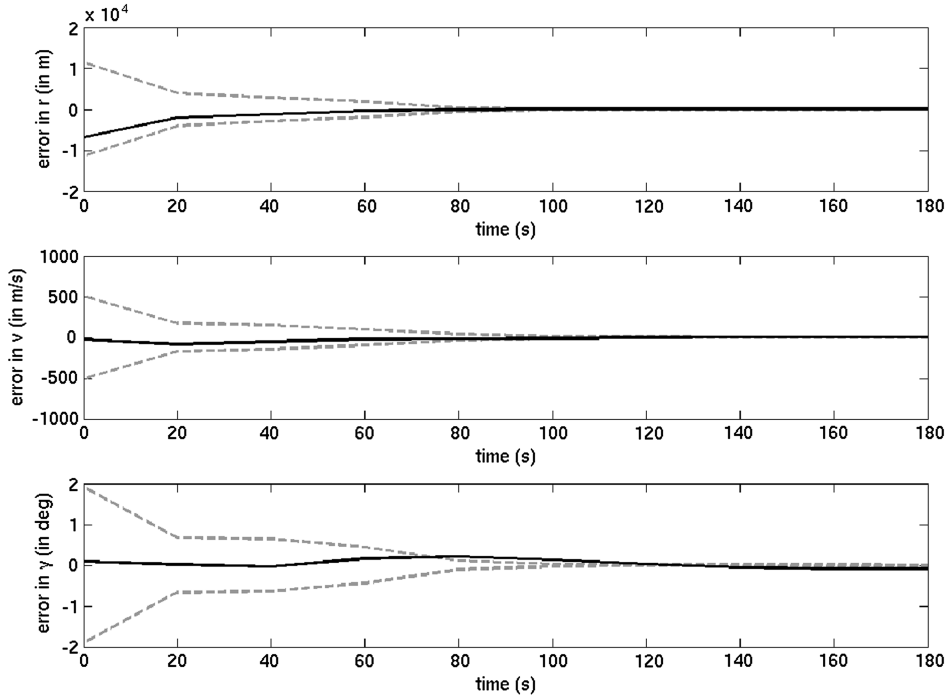

a) Plots for r, v and γ

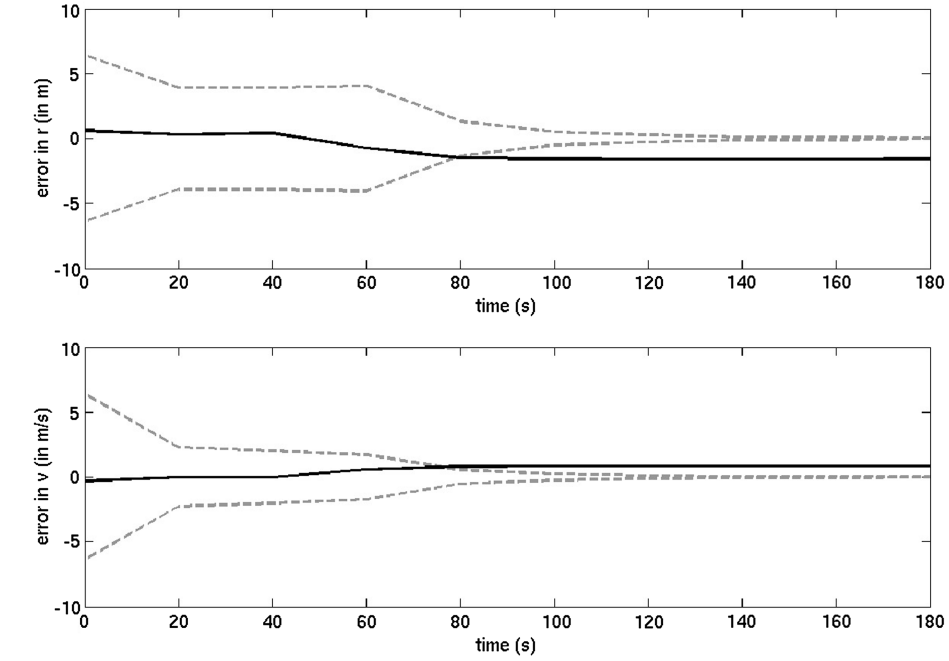

b) Plots for θ and λ

Fig. 23 Performance of the bootstrap filter with 9000 samples when applied to the six-state Vinh's equation. The dashed lines represent $\pm 3\sigma$ limits, and the solid lines represent the error in estimation.

$$\sigma_0 = \begin{pmatrix} 5.4\text{ km} & 0 & 0 & 0 & 0 \\ 0 & 3^\circ & 0 & 0 & 0 \\ 0 & 0 & 3^\circ & 0 & 0 \\ 0 & 0 & 0 & 240\text{ m/s} & 0 \\ 0 & 0 & 0 & 0 & 0.9^\circ \end{pmatrix} \quad (14b)$$

A nondimensionalized system is created, scaling each constant in Eq. (13) and using scaling constants given in Table 2. The normalization factors used for measurements are given in Table 5.

The performance of the FP operator-based filter is then compared with the generic particle filter and bootstrap filter when applied to the six-state Vinh's equation model. The initial states of the actual system are assumed to be

$$[R_m + 61\text{ km},\ -60.6^\circ,\ 30.3^\circ,\ 2.42\text{ km/s},\ -9.09^\circ,\ 0.0573^\circ]$$

in this case, with θ, λ, v, and γ having a 1% error in the initial state estimate. The measurement update interval is kept fixed at 20 s. Figure 21 show the plots for the FP operator-based filter with 9000 samples. Figures 22 and 23 show the plots for the generic particle filter and bootstrap filter, respectively, with the same number of samples. It can be seen that the FP operator-based estimator performs

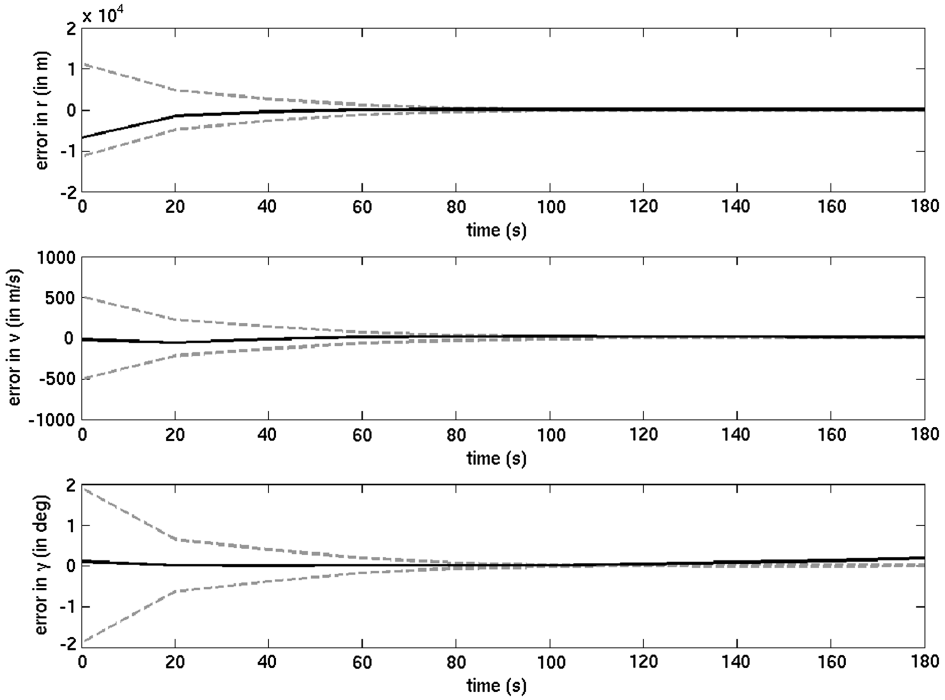

a) Plots for r, v and γ

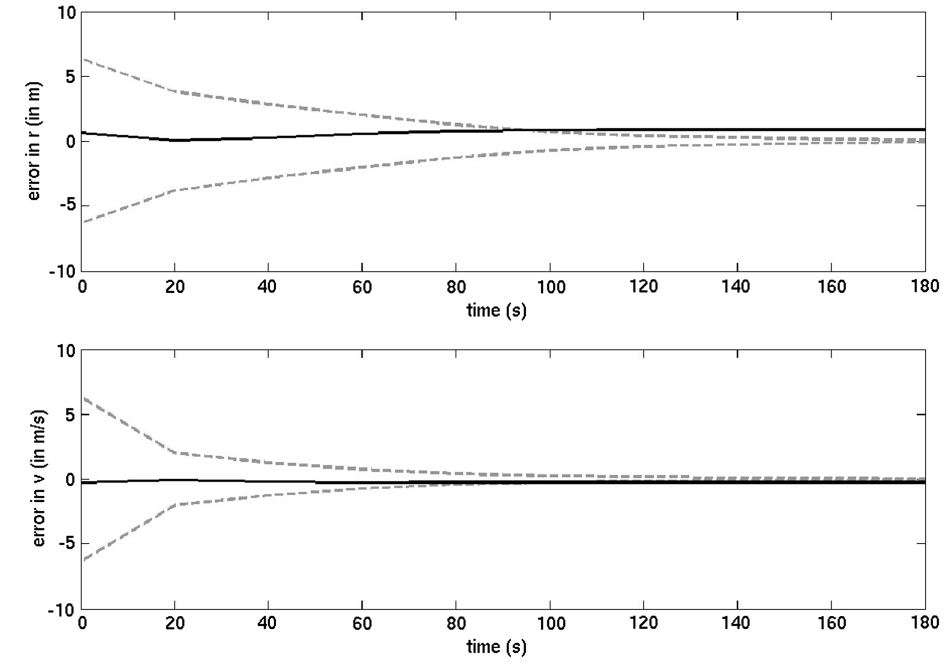

b) Plots for θ and λ

Fig. 24 Performance of generic particle filter with 30,000 samples when applied to six-state Vinh's equation. The dashed lines represent $\pm 3\sigma$ limits, and the solid lines represent the error in estimation.

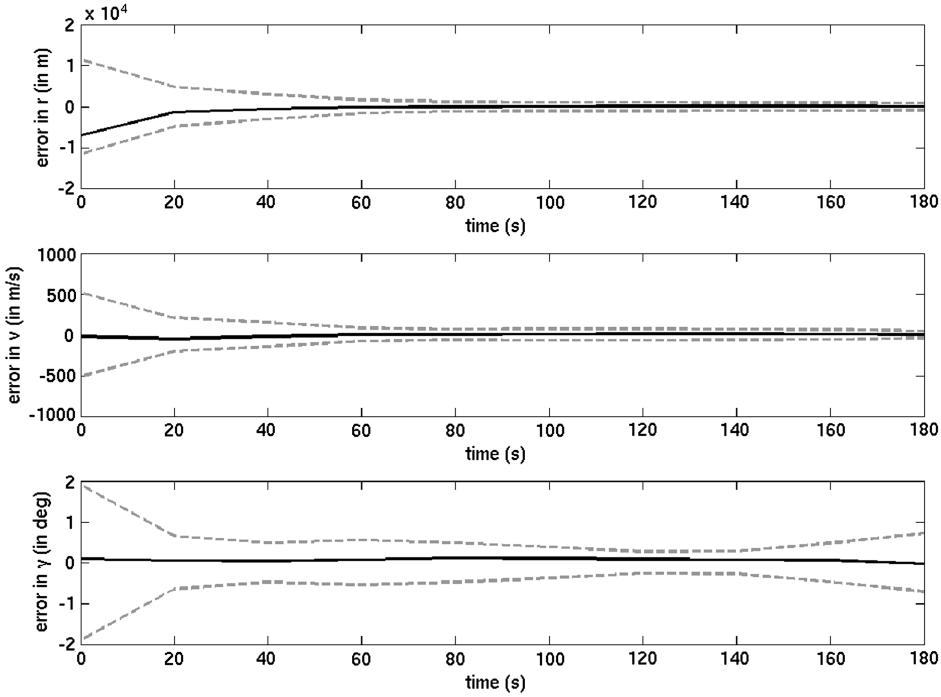

a) Plots for r, v and γ

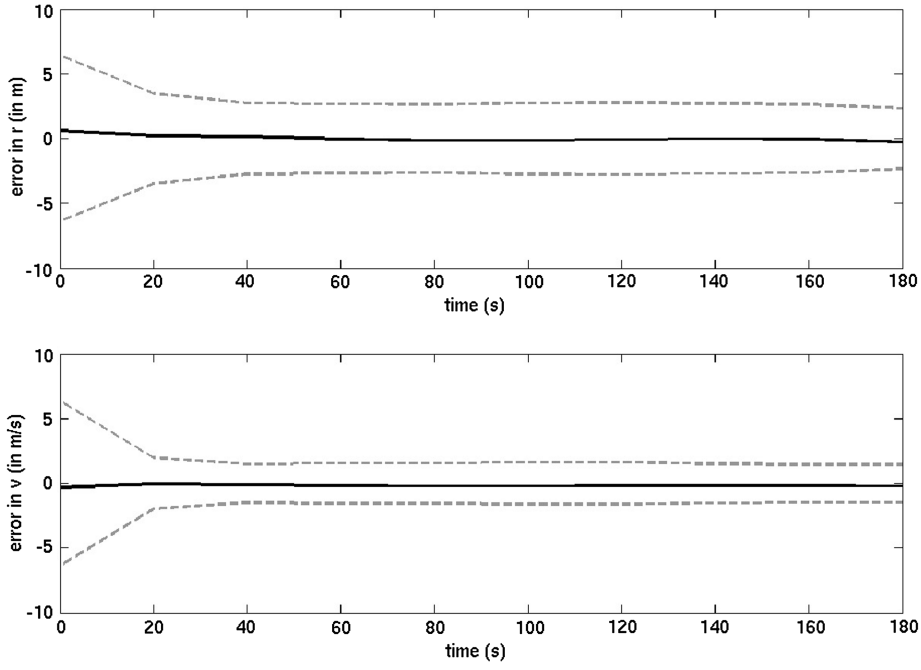

b) Plots for θ and λ

Fig. 25 Performance of the bootstrap filter with 25,000 samples when applied to the six-state Vinh's equation. The dashed lines represent $\pm 3\sigma$ limits, and the solid lines represent the error in estimation.

better than the particle filter-based estimators. The errors for the generic particle filter and the bootstrap filter diverge and are not inside the $\pm 3\sigma$ limits. Hence, these filters are inconsistent when the same number of samples as the FP operator are taken.

The best performances were those achieved using the particle filter and the bootstrap filter, shown in Figs. 24 and 25, respectively. The number of samples needed for the generic particle filter and the bootstrap filter are 30,000 and 25,000, respectively. For the particle filter, it is observed that, although the $\pm 3\sigma$ bounds converge, the estimation errors escape outside these limits. For the bootstrap filter, the errors and the $\pm 3\sigma$ limits converge, but for γ, the $\pm 3\sigma$ bounds diverge toward the end of the estimation period.

VI. Conclusions

In this paper, a nonlinear filtering algorithm based on the FP operator, or (equivalently) the Liouville equation, has been applied to a state-estimation problem related to atmospheric reentry problems. Two models are considered here. The first is the three-state Vinh's equation, and the sensor models used are dynamic pressure, heating rate, and flight-path angle. The second model is the six-state Vinh's equation, with measurements of the geocentric latitude and longitude taken along with the three measurements used in the three-state model. The superiority of the FP filter is demonstrated in comparison with the particle and bootstrap filters. It has been shown that for both

the three-state and six-state models, the FP operator-based filter achieves better results with a lesser number of samples than the particle-filter-based estimators; hence, it is computationally more efficient. However, it is important to note that this filter can only be used to resolve parametric uncertainty. For problems with process noise, a diffusion term has to be added to the Liouville equation. The PDE is then known as the Fokker–Planck–Kolmogorov equation. Our future efforts will be focused on addressing process noise in nonlinear filtering algorithms.

Acknowledgments

This research work was conducted under NASA funding from NASA Research Announcement NNH06ZEA001N-HYP, under cooperative agreement number NNX07AC44A: Fundamental Aeronautics: Hypersonics Project, Topic 5.4 Advanced Control Methods, Subtopic A.5.4.1 Advanced Adaptive Control, with Dan Moerder from NASA Langley Research Center as the technical monitor.

References

[1] Kalman, R. E., "A New Approach to Linear Filtering and Prediction Problems," *Journal of Basic Engineering*, Vol. 82, No. 1, 1960, pp. 35–45. doi:10.1109/ICASSP.1982.1171734

[2] Anderson, B., Moore, J. B., and Eslami, M., "Optimal Filtering," *IEEE Transactions on Systems, Man and Cybernetics*, Vol. 12, No. 2, 1982, pp. 235–236. doi:10.1109/TSMC.1982.4308806

[3] Evensen, G., "Using The Extended Kalman Filter with a Multilayer Quasi-Geostrophic Ocean Model," *Journal of Geophysical Research*, Vol. 97, No. C11, 1992, pp. 17,905–17,924. doi:10.1029/92JC01972

[4] Miller, R. N., Ghil, M., and Gauthiez, F., "Advanced Data Assimilation in Strongly Nonlinear Dynamical Systems," *Journal of the Atmospheric Sciences*, Vol. 51, No. 8, 1994, pp. 1037–1056. doi:10.1175/1520-0469(1994)051<1037:ADAISN>2.0.CO;2

[5] Gauthier, P., Courtier, P., and Moll, P., "Assimilation of Simulated Wind Lidar Data with a Kalman Filter," *Monthly Weather Review*, Vol. 121, No. 6, 1993, pp. 1803–1820. doi:10.1175/1520-0493(1993)121<1803:AOSWLD>2.0.CO;2

[6] Bouttier, F., "A Dynamical Estimation of Forecast Error Covariances in an Assimilation System," *Monthly Weather Review*, Vol. 122, No. 10, 1994, pp. 2376–2390. doi:10.1175/1520-0493(1994)122<2376:ADEOFE>2.0.CO;2

[7] Julier, S. J., and Uhlmann, J. K., "A New Extension of the Kalman Filter to Nonlinear Systems," *International Symposium on Aerospace/Defense Sensing, Simulation. and Controls*, Vol. 3, 1997, SPIE, Bellingham WA, pp. 182–193.

[8] Gordon, N. J., Salmond, D. J., and Smith, A. F. M., "Novel Approach to Nonlinear/Non-Gaussian Bayesian State Estimation," *IEE Proceedings F*, Vol. 140, No. 2, 1993, pp. 107–113. doi:10.1049/ip-f-2.1993.0015

[9] Arulampalam, M. S., Maskell, S., Gordon, N., and Clapp, T., "A Tutorial on Particle Filters for Online Nonlinear/Non-Gaussian Bayesian Tracking," *IEEE Transactions on Signal Processing*, Vol. 50, No. 2, 2002, pp. 174–188. doi:10.1109/78.978374

[10] Khalil, M., Sarkar, A., and Adhikari, S., "Nonlinear Filters for Chaotic Oscillatory Systems," *Nonlinear Dynamics*, Vol. 55, Nos. 1–-2, 2008, pp. 113–137. doi:10.1007/s11071-008-9349-z

[11] Glynn, P. W., and Iglehart, D. L., "Importance Sampling for Stochastic Simulations," *Management Science*, Vol. 35, No. 11, 1989, pp. 1367–1392. doi:10.1287/mnsc.35.11.1367

[12] Kitagawa, G., "Monte Carlo Filter and Smoother for Non-Gaussian Nonlinear State Space Models," *Journal of Computational and Graphical Statistics*, Vol. 5, No. 1, 1996, pp. 1–25. doi:10.2307/1390750

[13] Doucet, A., Godsill, S. J., and Andrieu, C., "On Sequential Monte Carlo Sampling Methods for Bayesian Filtering," *Statistics and Computing*, Vol. 10, No. 3, 2000, pp. 197–208. doi:10.1023/A:1008935410038

[14] Tanizaki, H., *Nonlinear Filters: Estimation and Applications*, Springer-Verlag, New York, 1996, pp. 17–111.

[15] Ristic, B., Arulampalam, S., and Gordon, N., *Beyond the Kalman Filter: Particle Filters for Tracking Applications*, Artech House, Norwood, MA, 2004, pp. 35–62.

[16] Doucet, A., De Freitas, N., and Gordon, N., *Sequential Monte Carlo Methods in Practice*, Springer-Verlag, New York, 2001, pp. 15–38.

[17] Daum, F., Huang, J., and Co, R., "Curse of Dimensionality and Particle Filters," *2003 IEEE Aerospace Conference, 2003, Proceedings*, IEEE Publ., Piscataway, NJ, 2003, pp. 41,979–41,993.

[18] Manohar, C. S., and Roy, D., "Monte Carlo Filters for Identification of Nonlinear Structural Dynamical Systems," *Sadhana Academy Proceedings In Engineering Sciences*, Vol. 31, No. 4, 2006, pp. 399–427. doi:10.1007/BF02716784

[19] Liu, J. S., and Chen, R., "Sequential Monte Carlo Methods for Dynamic Systems," *Journal of the American Statistical Association*, Vol. 93, No. 443, 1998, pp. 1032–1044. doi:10.2307/2669847

[20] Musso, C., Oudjane, N., and LeGland, F., "Improving Regularised Particle Filters," *Sequential Monte Carlo Methods in Practice*, Springer, New York, 2001, pp. 247–271.

[21] Gilks, W. R., and Berzuini, C., "Following a Moving Target Monte Carlo Inference for Dynamic Bayesian Models," *Journal of the Royal Statistical Society: Series B, Statistical Methodology*, Vol. 63, No. 1, 2001, pp. 127–146. doi:10.1111/1467-9868.00280

[22] Snyder, C., Bengtsson, T., Bickel, P., and Anderson, J., "Obstacles to High-Dimensional Particle Filtering," *Monthly Weather Review*, Vol. 136, No. 12, 2008, pp. 4629–4640. doi:10.1175/2008MWR2529.1

[23] Casella, G., and Robert, C. P., "Rao–Blackwellisation of Sampling Schemes," *Biometrika*, Vol. 83, No. 1, 1996, p. 81. doi:10.1093/biomet/83.1.81

[24] Daum, F., and Co, R., "Nonlinear Filters: Beyond the Kalman Filter," *IEEE Aerospace and Electronic Systems Magazine*, Vol. 20, No. 8, Part 2, 2005, pp. 57–69. doi:10.1109/MAES.2005.1499276

[25] Lasota, A., and Mackey, M. C., *Chaos, Fractals, and Noise: Stochastic Aspects of Dynamics*, Springer, New York, 1994, p. 213, Chap. 1, pp. 187–247.

[26] Kubo, R., "Stochastic Liouville Equations," *Journal of Mathematical Physics*, Vol. 4, No. 2, 1963, pp. 174–184. doi:10.1063/1.1703941

[27] Risken, H., *The Fokker–Planck Equation: Methods of Solution and Applications*, Springer-Verlag, New York, 1996, pp. 63–91.

[28] Runolfsson, T., and Lin, C., "Computation of Uncertainty Distributions in Complex Dynamical Systems," *Proceedings of the 2009 American Control Conference*, IEEE Press, Piscataway, NJ, 2009, pp. 2458–2463.

[29] Halder, A., and Bhattacharya, R., "Beyond Monte Carlo: A Computational Framework for Uncertainty Propagation in Planetary Entry, Descent and Landing," AIAA Guidance Navigation and Control Conference, Toronto, ON, AIAA Paper 2010-8029, 2010.

[30] Daum, F., and Krichman, M., "Non-Particle Filters," *Proceedings of the SPIE*, Vol. 6236, SPIE, Bellingham, WA, 2006, Paper 623614.

[31] Daum, F., Krichman, M., Co, R., and Woburn, M. A., "Meshfree Adjoint Methods for Nonlinear Filtering," *2006 IEEE Aerospace Conference*, IEEE Publ., Piscataway, NJ, 2006. doi:10.1109/AERO.2006.1655925

[32] Daum, F., and Huang, J., "Particle Flow for Nonlinear Filters with Log-Homotopy," *Proceedings of the SPIE*, Vol. 6969, SPIE, Bellingham WA, 2008, Paper 696918.

[33] Daum, F., and Huang, J., "Nonlinear Filters with Particle Flow Induced by Log-Homotopy," *Proceedings of the SPIE*, Vol. 7336, SPIE, Bellingham WA, 2009, Paper 733603.

[34] Egorov, J. V., Subin, M. A., Agranovic, M. S., and Fedorjuk, M. V., *Partial Differential Equations IV: Microlocal Analysis and Hyperbolic Equations*, Springer-Verlag, New York, 1993, pp. 151–173.

[35] Halton, J. H., "On the Efficiency of Certain Quasi-Random Sequences of Points in Evaluating Multi-Dimensional Integrals," *Numerische Mathematik*, Vol. 2, No. 1, 1960, pp. 84–90. doi:10.1007/BF01386213

[36] Nobile, F., Tempone, R., and Webster, C. G., "A Sparse Grid Stochastic Collocation Method for Partial Differential Equations with Random Input Data," *SIAM Journal on Numerical Analysis*, Vol. 46, No. 5, 2008, pp. 2309–2345. doi:10.1137/060663660

[37] Zenger, C., "Sparse Grids," *Proceedings of the Research Workshop of the Israel Science Foundation on Multiscale Phenomenon, Modelling and Computation*, Eliat, Israel, March 1997, p. 86.

[38] Bungartz, H. J., and Griebel, M., "Sparse Grids," *Acta Numerica*, Vol. 13, 2004, pp. 147–269.
doi:10.1017/S0962492904000182

[39] Becker, R., and Rannacher, R., "An Optimal Control Approach to A Psteriori Error Estimation in Finite Element Methods," *Acta Numerica*, Vol. 10, 2003, pp. 1–102.
doi:10.1017/S0962492901000010

[40] Giles, M. B., and Uli, E. S., "Adjoint Methods for PDEs: A Posteriori Error Analysis and Postprocessing by Duality," *Acta Numerica*, Vol. 11, 2002, pp. 145–236.
doi:10.1017/CBO9780511550140.003

[41] Bangerth, W., and Rannacher, R., *Adaptive Finite Element Methods for Differential Equations*, Birkhäuser, Boston, 2003, pp. 15–69.

[42] Bayes, T., "An Essay Towards Solving a Problem in the Doctrine of Chances: By the Late Rev. Mr. Bayes, F.R.S. Communicated by Mr. Price, in a Letter to John Canton, A.M.F.R.S.," *Philosophical Transactions of the Royal Society of London*, Vol. 53, 1763, pp. 370–418.
doi:10.1098/rstl.1763.0053

[43] Bryson, A. E., and Ho, Y. C., *Applied Optimal Control: Optimization, Estimation, and Control*, Hemisphere, New York, 1975, pp. 348–388.

[44] Chern, J.-S., and Vinh, N. X., "Optimal Reentry Trajectories of a Lifting Vehicle," NASA, CR 3236, 1980.

[45] Bollino, K. P., Ross, I. M., and Doman, D. D., "Optimal Nonlinear Feedback Guidance for Reentry Vehicles," AIAA Guidance Navigation and Control Conference and Exhibit, Keystone, CO, AIAA Paper 2006-6074, 2006.

[46] Sengupta, P., and Bhattacharya, R., "Uncertainty Analysis of Hypersonic Flight Using Multi-Resolution Markov Operators," AIAA Guidance Navigation and Control Conference and Exhibit, Honolulu, HI, AIAA Paper 2008-6298, 2008.